The Abdus Salam
International Centre for Theoretical Physics

United Nations
Educational, Scientific and
Cultural Organization

IAEA
International Atomic Energy Agency

2167-3

Advanced School on Direct and Inverse Problems of Seismology

27 September - 9 October, 2010

Surface Wave Earthquake and Ambient Noise Tomography Applications: Inversion for Shear Velocity and Attenuation Models and Location

A.L. Levshin
University of Colorado
Boulder
USA

A. L. Levshin

University of Colorado, Boulder, USA

Lecture 3

Surface Wave Earthquake and Ambient Noise Tomography
Applications: Inversion for Shear Velocity and Attenuation Models, and Location

Step 1. Surface Wave Earthquake Tomography

1.1. Measurements

We measure the group velocities using frequency-time analysis (FTAN) (Levshin et al., 1989) described in the previous lecture.

Global tomography

For global tomography we used broadband waveforms following earthquakes that occurred from 1977 - 2002 at stations from both global networks (GDSN, GSN, GEOSCOPE, GEOFON), regional arrays (MEDNET, Canadian Network, KNET, KAZNET, POSEIDON) as well as temporary regional arrays (e.g., Saudi Arabian Network, SKIPPY in Australia, PASSCAL deployments in Tibet, South America, Antarctica, and South Africa). The phase velocities were measured at Harvard University and Utrecht University, separately. These phase velocity data sets are described by Ekström (1997) and Trampert & Woodhouse (1995). We merged all phase velocity measurements into a single data set. A cluster analysis, i.e. combining many similar paths into one "common" path, is applied to both the group and phase velocity measurements for out-lier rejection and *Rms* estimation. The results of this analysis show that typical measurement errors are 20 - 25 m/s for group velocities, except for very short periods, and 10 - 15 m/s for phase velocities, except for long period Love waves.

Data coverage is generally better for Rayleigh waves than for Love waves, is better at intermediate than at very short or very long periods, and is better in the northern than in the southern hemisphere. This heterogeneous data coverage is imposed by the distribution of receiving stations and earthquakes. Data coverage optimizes in Eurasia and is currently worst across Africa, the central Pacific, parts of the Indian Ocean, and Antarctica (Figure 1). The whole data set consists of more than 200,000 group velocity and 50,000 phase velocity paths.

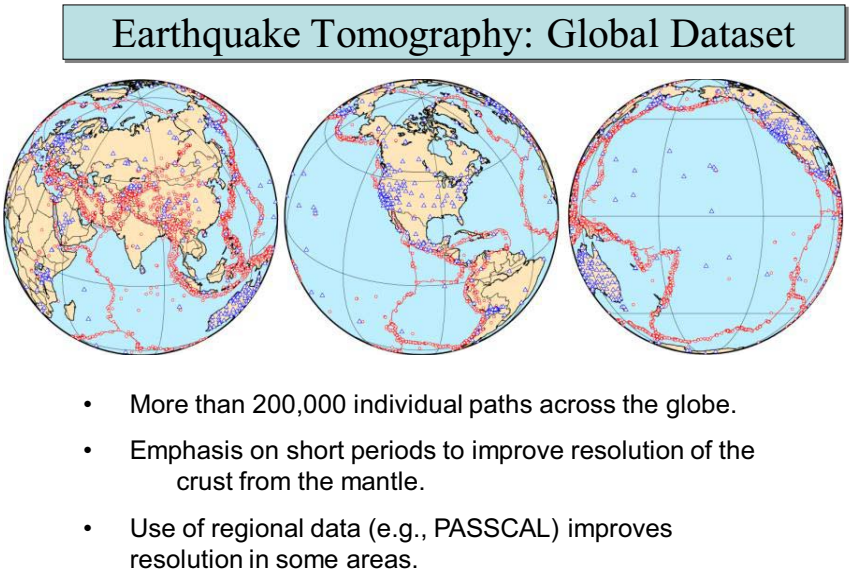

Figure 1: Events and stations selected for global tomography.

Regional tomography

As an example of the regional tomography I will show results of the work of a joint team: CU-B, NORSAR, and University of Oslo on the crustal-upper mantle structure of the Barents Sea (Levshin et al., 2006). To improve the data coverage in the target region, we have extensively searched for long period and broadband data from seismic stations and arrays in the European Arctic, including local networks and temporary array installments. We were able to retrieve surface waveform data and make surface wave dispersion observations on data from archives at NORSAR, University of Bergen, the Kola Science Center in Apatity, the Geological Survey of Denmark and the University of Helsinki, in addition to data retrievable from the international data centers at IRIS and GEOFON. An overview map of the station locations is in Fig. 2 (top left). New Love- and Rayleigh-wave data were identified for more than150 seismic events (including 25 nuclear tests at Novaya Zemlya and 13 so-called Peaceful Nuclear Explosions (PNEs) within the former Soviet Union) spanning a time period from 1971 to 2005. Fig. 2 (bottom left) shows the geographic distribution of these events. The PNE have not been used previously for surface wave studies. Wave paths for 20 s and 40 s Rayleigh waves are shown at the right part of Figure 2.

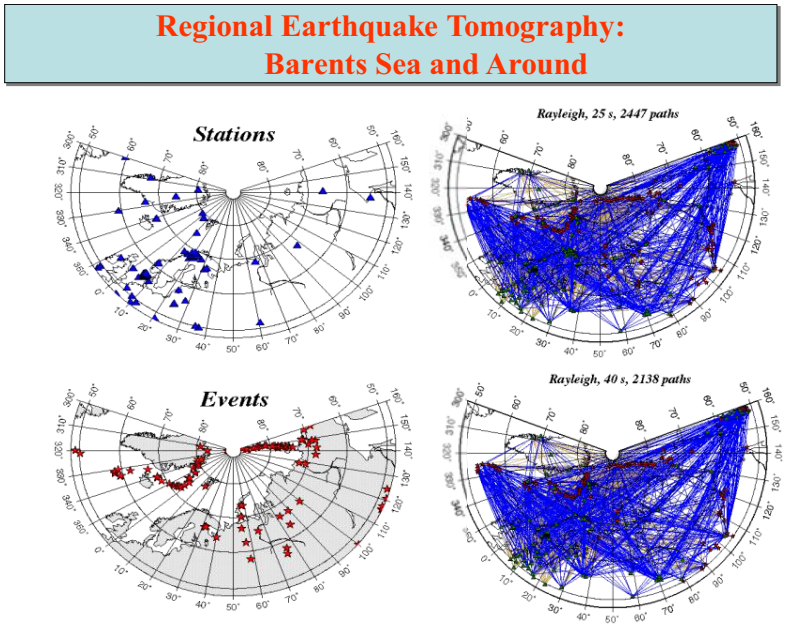

Figure 2: Events, stations and wave paths for regional group velocity tomography (Barents Sea).

1.2 Surface wave tomography

In the first step, the processed group and phase velocity dispersion measurements for each wave type (Rayleigh, Love) and period are converted to 2-D dispersion maps. We construct maps on a 2°by2° grid world-wide in the following period bands: group velocity, 16 - 200 s; phase velocity, 40 - 150 s. These maps typically fit the measured group velocities with *Rms* misfits of 40 - 50 m/s and the measured phase velocities to 20 - 40 m/s, or about twice the measurement error. Historically we used two methods for tomographic inversion.

Both methods are based on a grid representation of the earth model and triangular interpolation between grid points. Both methods try to minimize the difference between observed and predicted by the model travel times along epicenter-station paths. Both methods start search from a reference model and include damping and regularization as well as special constraints for zones of the map poorly covered by observations. The difference between methods is in the definition of surface wave rays. The first method which we call "Gaussian Tomography" defines the ray as a stripe on a sphere centered around the great circle paths with the sensitivity to the structure decreasing with the distance d from the central ray as $\exp(-d^2/2\sigma^2)$ (Figure 3). We use values of σ that vary with period and wave type from ~200 to 350 km, so the full-width of the ray at 10% of the maximum amplitude is about 6σ; i.e., it varies from about 1200 to 2100 km from short to long periods.

However, this is a crude approximation to the real scattering of the wave which is epicentral distance and period depending. To make it more realistic it is necessary to introduce the estimates of ray sensitivity based on scattering theory. The simplest way to do it is to estimate the width of the first Fresnel zone along the ray of given period. We call this tomographic

technique "Diffraction Tomography". The region over which surface waves scatter is defined by an ellipse on a sphere given by the equation

$$|\Delta - (\Delta_1 + \Delta_2)| = \lambda/N$$

as shown in Figure 3, where λ is the wavelength of the wave of interest determined from PREM (Dziewonski & Anderson, 1981).

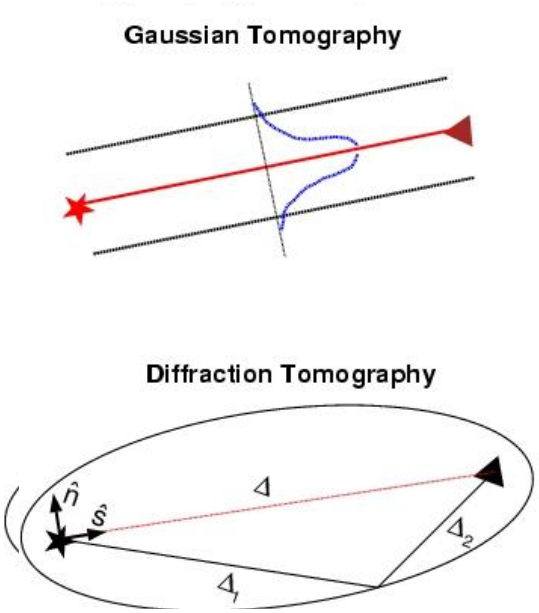

Figure 3: Schema explaining two tomographic techniques.

The first Fresnel-zone encompasses all scatterers whose combined distance from the source and receiver is less than half a wavelength. This corresponds to all signals that will arrive within half a period of the first arrival, and in this case $N = 2$. The width of this zone increases as the source-receiver geodetic distance grows.

The optimal value of N to model the scattering sensitivity of surface waves on a sphere remains the subject of debate. Yoshizawa & Kennett (2002) argue that the primary "zone of influence" spans only about one-third of the width of the first Fresnel-zone, so $N = 18$ is the value that should be used in surface wave tomography. Spetzler et al. (2001) argue that $N = 8/3$ is the value that is consistent with the Born/Rytov approximation. To retain consistency with the Born/Rytov approximation we use $N = 8/3$ here. We refer to the region so defined as the "sensitivity-zone", which is a subset of the first Fresnel zone. Dahlen & Zhou (2006), Zhou et al. (2005,2006), Nolet (2008) describes the more strict approach called frequency-dependent tomography where ***space*** sensitivity kernels are calculated from Born approximation. Sensitivity-zone widths, irrespective of the choice of N, grow with period and path, as illustrated by Figure 4.

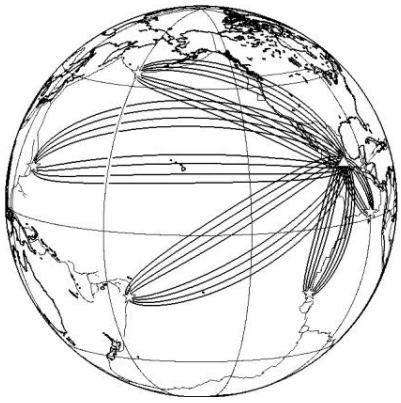

Figure 4: Rayleigh wave sensitivity-zones (N = 8/3) for waves observed in Mexico (triangle) originating from several epicentral regions (stars): Galapagos (2087 km), East Pacfic Rise (4493 km), Aleutians (7777 km), Tonga (8916 km), and the Marianas (11700 km). These sensitivity-zones are for 20 s, 50 s, 100 s, and 150 s Rayleigh waves, where the zone is narrowest at shortest period.

The detailed description of the first method is given in Barmin et al. (2001), and of the second method in Ritzwoller et al., (2002). Examples of group velocity maps are shown in Figures 5 and 6.

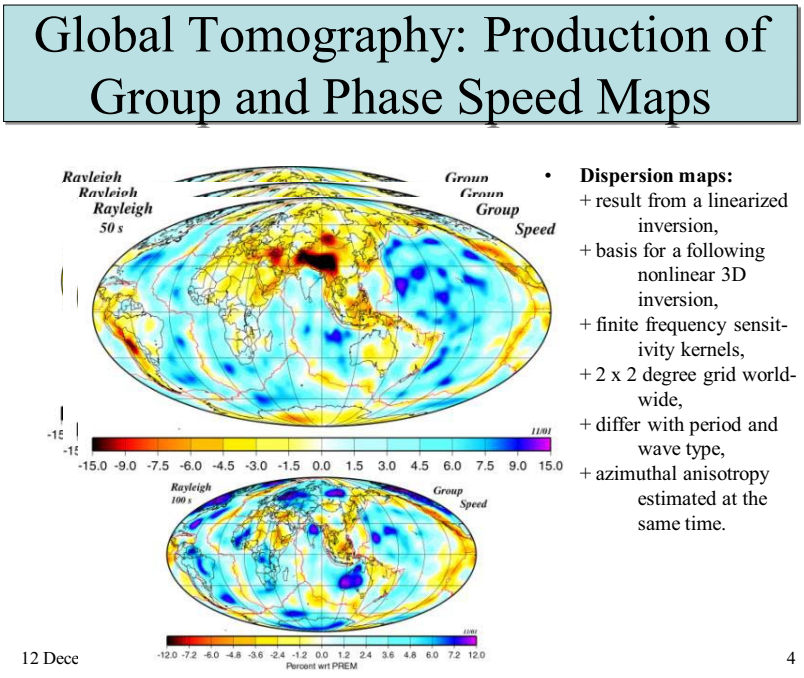

Figure 5: Examples of 2-D global tomography.

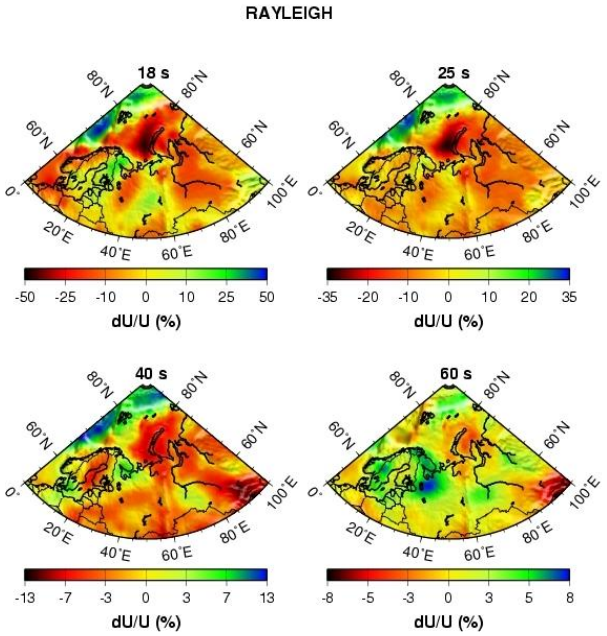

Figure 6: Examples of 2-D regional tomography (Barents Sea).

Step 2. The inversion of the tomographic maps for a shear velocity model

This inversion is a multi-stage process that culminates in a Monte-Carlo inversion for an ensemble of acceptable models at each spatial node. The middle of the ensemble (\Median Model") together with the half-width of the corridor defined by the ensemble summarize the results of the inversion. The most robust features of the resulting model are those that appear in every acceptable model. We refer to these features as “persistent" and identify them as the features of the model that are most worthy of interpretation. In regions of poor data coverage the tomographic maps and the median shear velocity model will revert to a common reference (the “Initial Model" defined below) while the uncertainties will grow up to limits imposed by a-priori constraint.

2.1. Data for Inversion

The data are surface wave group and phase velocities. Although phase ($C = \omega/k$) and group ($U = d\omega/dk$) velocities are simply related by

$$U = \frac{C}{1 - \frac{\omega}{C(\omega)} \frac{dC}{d\omega}}$$

the simultaneous inversion of U and C is substantially better than the use of either alone, as Figure 7 suggests.

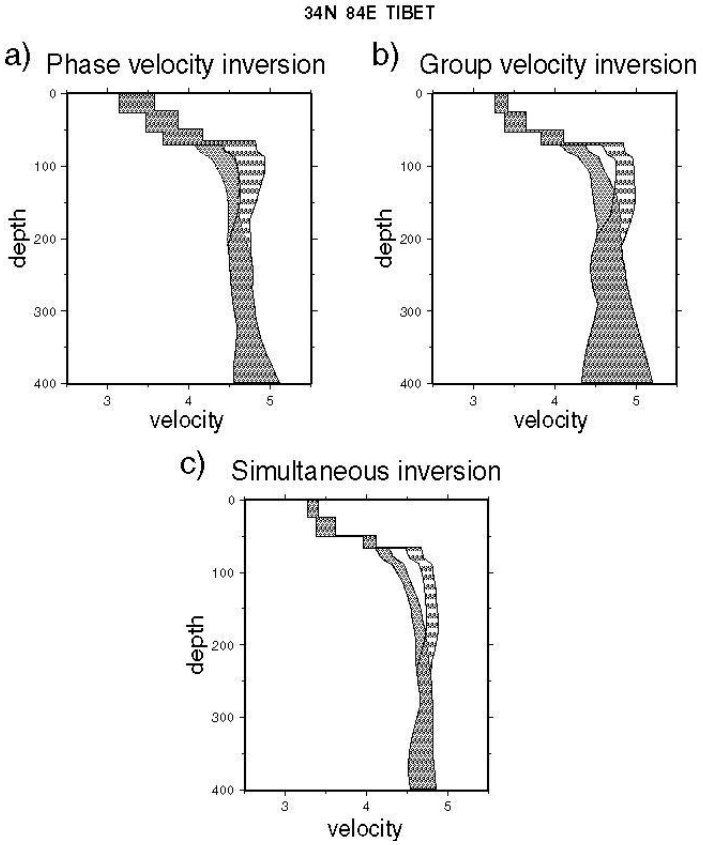

Figure 7: Examples of inversions at a point located in Tibet illustrating the relative importance of phase and group velocities: (a) inversion of the phase velocities only, (b) inversion of the group velocities only, (c) inversion of the whole data-set. The corridor of accepted SV velocities is plotted in gray and for SH velocities with horizontal hatching.

There are two reasons for this. First, the group velocity measurements extend to much shorter periods than the phase velocities and, therefore, provide unique constraints on shallow structures that help to resolve the trade-off between crustal and mantle structures in the inversion. This effect is amplified by the fact that group velocities are sensitive to shallower structures than phase velocities at a given period. Second, phase and group velocities are measured differently. Group velocities are measured on the amplitude of the surface wave packet and phase velocities on the phase, so the error processes in the measurements are largely independent.

The global 3-D model CUB 2 obtained in result of inversion is presented at the webpage http://ciei.colorado.edu/~nshapiro/MODEL. Examples of depth slices of this model are shown in Figure 8.

The inversion of this kind of 2-D tomographic maps permits to estimate the strength of radial anisotropy in the upper mantle (Shapiro & Ritzwoller, 2002). Analysis of surface wave data for evaluating radial anisotropy is discussed by Smith & Dahlen (1973), Nataf et al.(1986), Montagner et al., 1988,1989,1991; Montagner 1994, 1998) . This subject will be discussed in lectures by Prof. Montagner here.

Global 3-D model

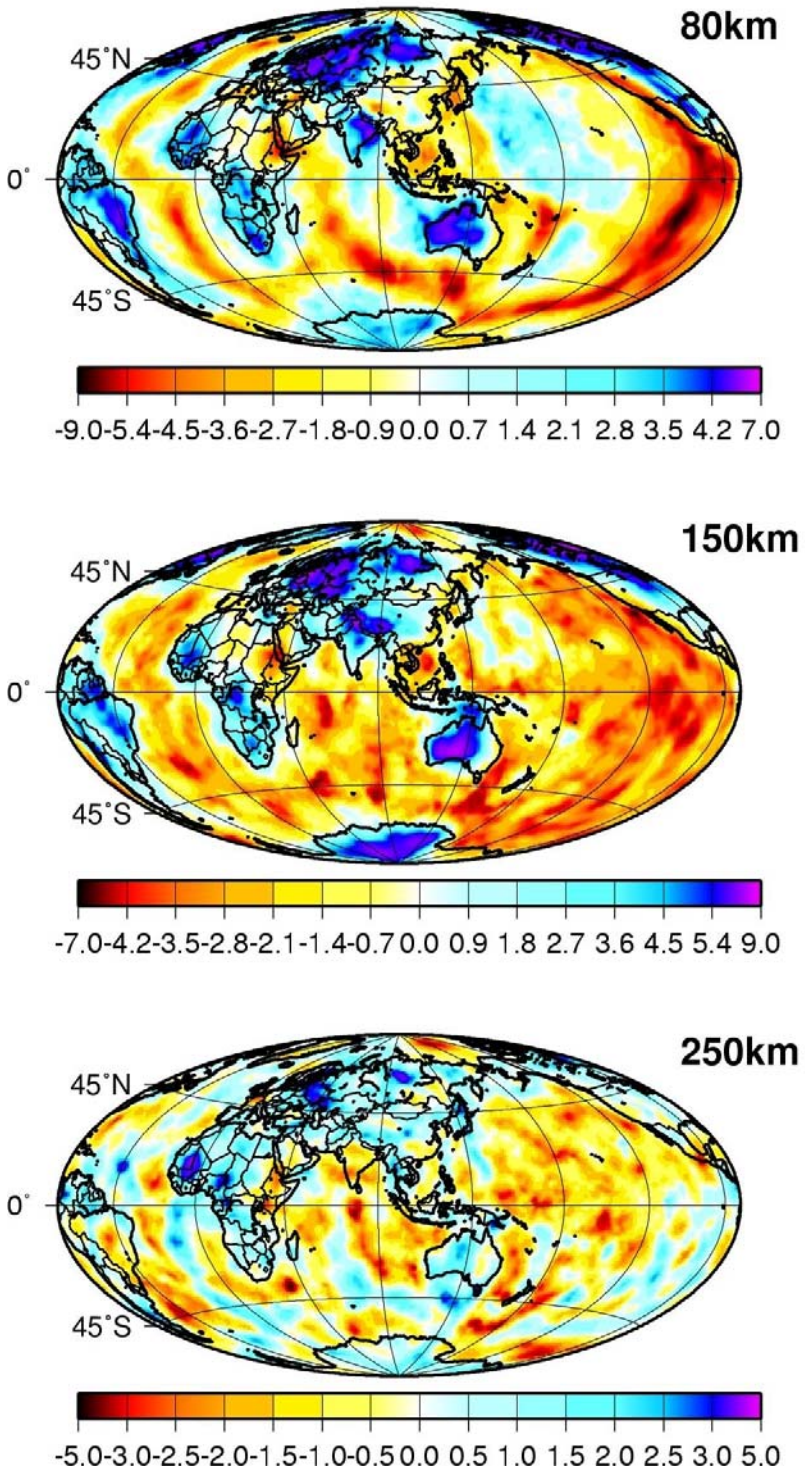

Figure 8: Depth slices of the 3-D shear velocity model CUB2 relative to the 1-D model AK-135 (Kennett et al., 1995).

Application of a 3-D global model to improve regional event locations

Accurate location of weak seismic events is crucial for monitoring clandestine nuclear tests, for studying local seismic structures, and for assessing possible seismic hazards. Outside of a few regions with dense seismic networks, weak seismic events (with magnitude less than 4) are usually sparsely recorded at epicentral distances less than 20^o. Because of lateral variations in crustal and upper mantle structures, observed travel times of seismic phases deviate significantly from predictions based on 1-dimensional (1-D) seismic models. Accurately locating weak seismic events remains a difficult task for modern seismology. Perhaps the most promising solution to this problem is the use of a 3-dimensional (3-D) model of the Earth.

Conversion of -3D S velocity model to 3-D P velocity model

As P waves play dominant role in any location technique it is necessary to convert the obtained S velocity model of the mantle into P velocity model. There are two general approaches to doing this. The first is to use “empirical scaling relations" that convert S-wave anomalies into P-wave anomalies. The most successful of these, map shear-speed perturbations, δv_s, relative to a reference S-model, v_{s0} , to compressional-velocity perturbations, δv_p, relative to a reference P-model, v_{p0} , where $d \ln v_p / d \ln v_s$ is then taken to be an empirically constrained constant that may be a function of depth, but is usually depth invariant. The second approach which we prefer is to use a “theoretical conversion" based on laboratory measurements of thermoelastic properties of mantle minerals and on models of the average mineralogical composition of the mantle. We convert only isotropic v_s to v_p. In the radially anisotropic part of CUB2.0 we, therefore, use $(v_{sv} + v_{sh})=2$.

Location experiment

Here we present the results of a validation test in which, using the described above 3-D model of the crust and upper mantle and regional phase data alone, we relocate ~340 earthquakes and nuclear explosions in Eurasia. The event locations using the 3-D model are compared with so-called Ground Truth (GT) data, either known by non-seismic means or validated by cluster analysis, with location accuracy mostly 5 km or better. To locate seismic events using only regional Pn and P phases we apply the grid-search technique. A grid 50x50 km with 1 km spacing is built around a reference point known from teleseismic information taken from PDE or EHB (Engdahl et al.,1998) catalogs. For each point of the grid and each observed arrival we calculate travel times of Pn and P waves as predicted by our model. Travel times for each phase are found using so-called Source-Specific Station Corrections (SSSCs) which were calculated beforehand for more than 800 seismic stations. Each SSSC is a multi-level table of travel times for Pn and P waves propagating in our 3-D model, each level corresponds to a certain source depth and contains travel times on a grid of azimuthal directions from the station to epicentral distances less than 20^o. Actually, there are not full travel times but corrections relative to 1-D model (typically, AK135). These corrections are found by 2-D ray tracing through the 3-D model using technique developed by Červeny & Pšenčik (1984). An example of SSSC is shown in Figure 9.

We estimate *Rms*-misfit of predicted and observed travel times for all observed phases in each point of the grid and select the node with minimal rms as a new location (Figure 10). Location errors for 3-D and 1-D location for explosions on Lop Nor test site in China and earthquakes in Racha seismic zone, Georgia, relative to ground truth locations are shown in Figure 11. One can see strong bias in locations with 1-D model.

The statics of relocation for a set of 16 clusters shows significantly better accuracy achieved using 3-D location. Results of random selection experiment in which we use for relocation different combinations of *n* stations for different values of *n* show that 3-D location produces more accurate results than 1-D location in 70-75% of all cases (for explosions and GT5 earthquakes), if $n \geq 5$. This test indicates that the location of regional events can be significantly improved by using a global 3-D model. More details are presented in Levshin & Ritzwoller (2002), Ritzwoller et al. (2002b).

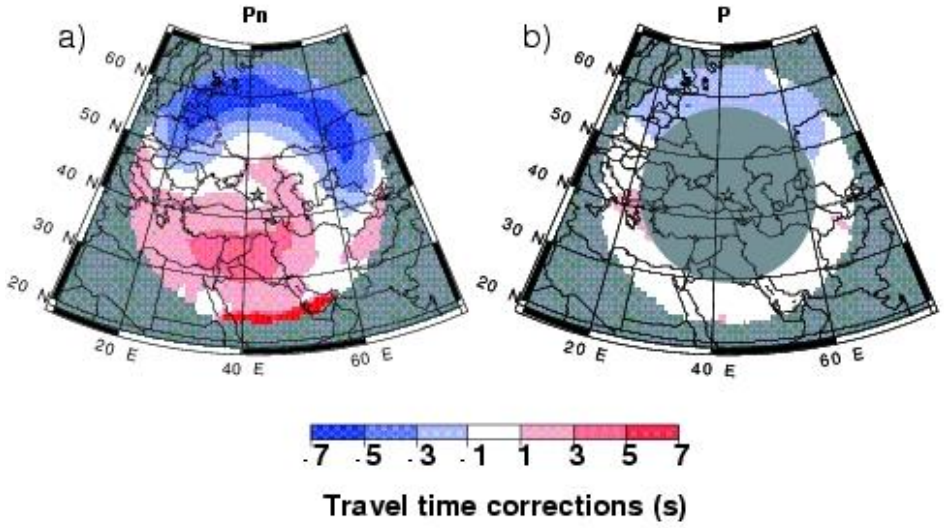

Figure 9: Example of Pn and P travel time correction surfaces computed for a surface source for station KIV. The corrections here are relative to the 1-D model AK135.

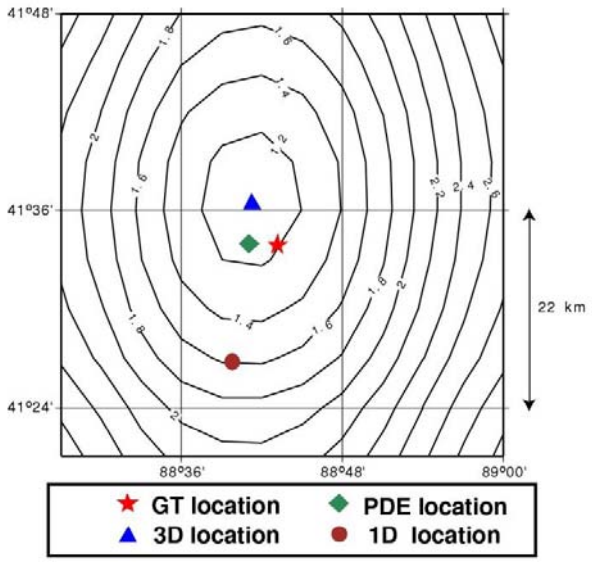

Figure 10: Contours of *Rms*-misfit using the 3-D model CUB2.0 TH for a grid of hypothesized epicenters for an explosion at the Lop Nor test site (May 26, 1990; 54 reporting stations). Units are seconds.

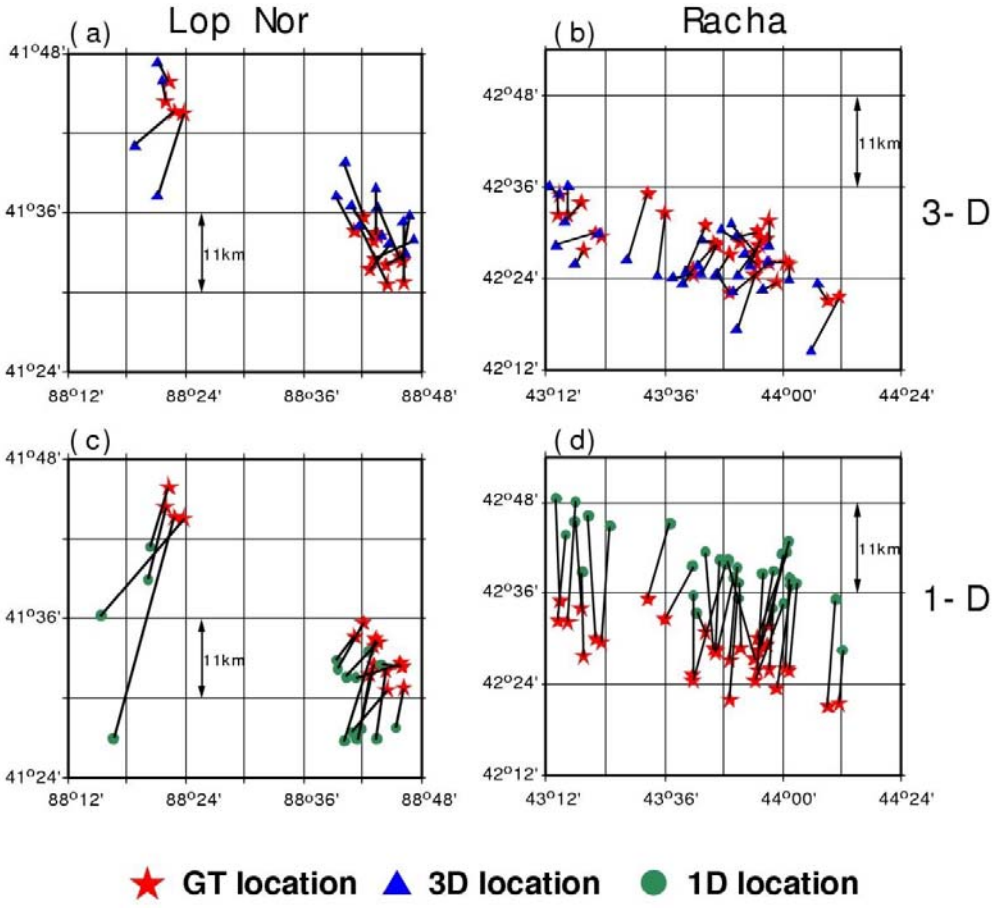

Figure 11: Mislocation vectors from two event clusters for (left column) explosions on the Lop Nor test site and (right column) earthquakes near Racha, Georgia. (a) and (b) 3-D model (CUB2.0) locations. (c) and (d) 1-D model (AK135) locations. Stars mark GT locations, triangles and circles are 3-D and 1-D model locations, respectively.

An Example of a Regional 3-D model

As an example of a regional 3-D model I show the Barents Sea model obtained from the surface wave tomography (Levshin et al., 2007). The shear-velocity slice and directions of several transects across the region are shown in Figure 12a. Shear-velocity cross-sections along these transects are shown in Figure 12b. This 3-D model, BARMOD, reveals substantial variations in shear wave speeds in the upper mantle across the region with a nominal resolution of $1^{\circ} \times 1^{\circ}$. Of particular note are clarified images of the mantle expression of the continent-ocean transition in the Norwegian Sea and a deep, high wave speed lithospheric root beneath the Eastern Barents Sea, which presumably is the remnant of several Palaeozoic collisions.

(a)

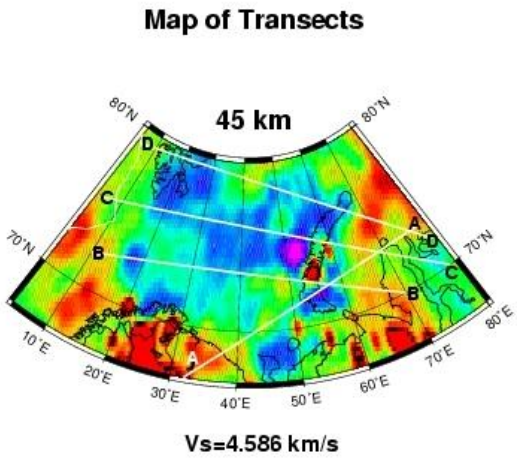

(b)

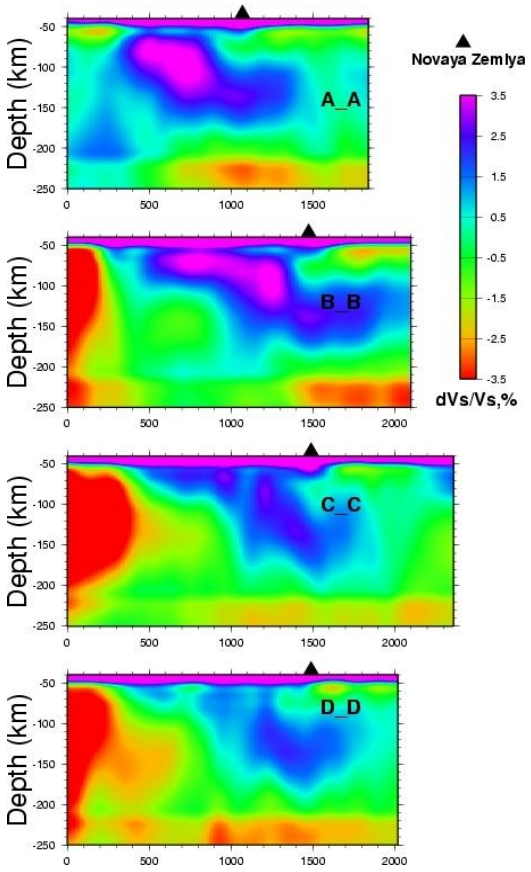

Figure 12: Depth slice and cross-sections along transects of BARMOD shear velocity model.

Surface Wave Attenuation Tomography

Surface wave observations can be used for construction of 2-D and 3-D attenuation models of the crust and upper mantle. I present here a recent attenuation model for midperiod Rayleigh waves in Central Asia and surrounding regions (Levshin et al., 2010). This model is defined by maps of attenuation coefficient across the region of study in the period band 14-24 s. The model is constructed to characterize the regional variations in attenuation of seismic waves in the crust, which are related to the tectonic history of the studied territory, to calibrate the regional surface-wave magnitude scale, and to extend the teleseismic 'surface-wave magnitude – body-wave magnitude' (*Ms-mb*) discriminant to regional distances.

The construction of the model proceeds in three stages. The first stage in model construction is the measurement of Rayleigh wave spectral amplitudes. We collected and processed waveform data for 200 earthquakes occurring from 2003 to 2006 inside and around Eurasia, and used records of about 135 broadband permanent and temporary stations. This data set provided a sufficient number of spectral amplitude measurements between periods T=14 - 24 s for the construction of two–dimensional tomographic maps of attenuation coefficients γ_R and corresponding Q_R-values (where $Q_R = \pi/(2TU_R)$). At the second stage of the work, the integral of attenuation coefficients along given paths is estimated using both inter-station measurements and single-station measurements corrected for source and receiver terms. The third stage includes the refining of source parameters, recalculation of attenuation coefficient integrals after this refinement, grooming of resulting coefficients, and multi-stage tomograhic inversion of the data.

Tomographic maps for the set of periods from 14 to 24 s, which exhibit clear correlation with geology and tectonics of the territory under study are shown in Figures 13 and 14. Validation of these maps using the inter-station measurements confirms their accuracy in predicting the observations.

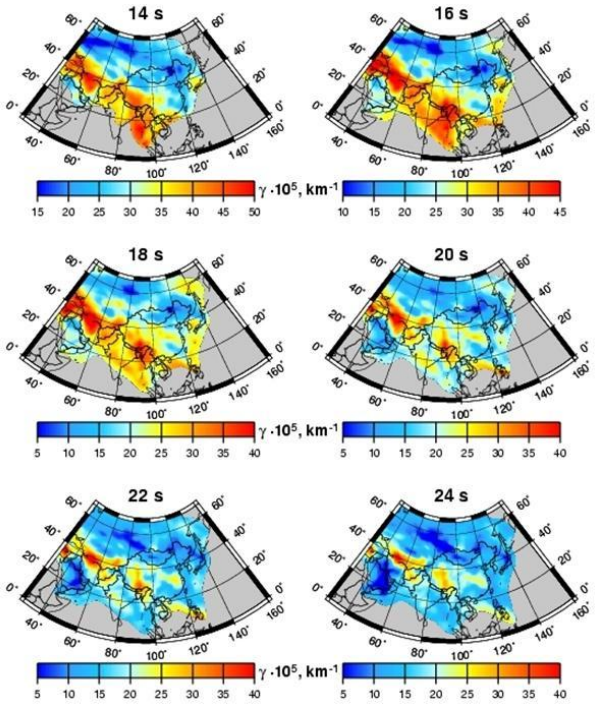

Figure 13: Maps of attenuation coefficient γ_R of Rayleigh waves at indicated periods.

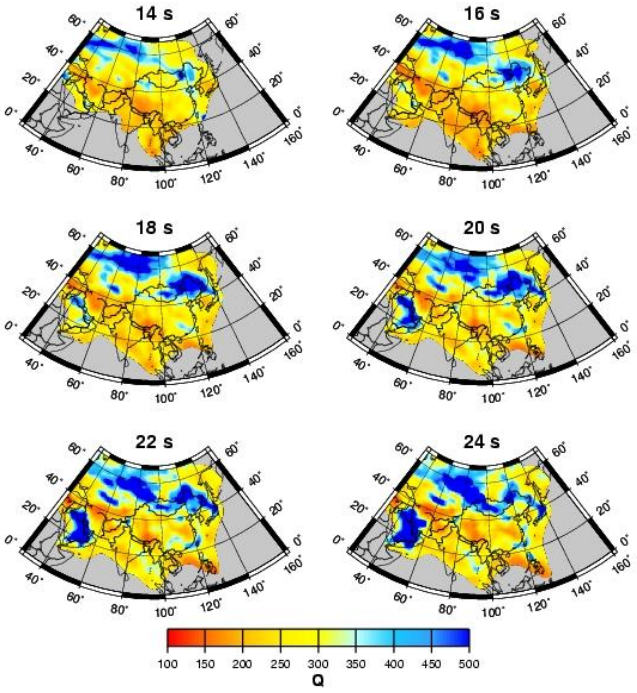

Figure 14: Maps of parameter Q_R of Rayleigh waves at indicated periods.

You will hear more about attenuation studies in lectures of Prof. Mitchell.

Seismic Tomography Using Ambient Seismic Noise

Surface-wave tomography based on use of earthquakes and explosions has serious limitations due to the existing pattern of seismicity: strong enough events occur only in certain places and are sparse in time. During recent years seismologists following theoretical results (e.g., Weaver & Lobkis, 2001; Snieder, 2004) developed a new tomographic technique based on use of ambient seismic noise. Interferometry technique using ambient seismic noise are widely used now and yield detailed information about the Earth's structure. I illustrate some of these developments by examples of surface-wave seismological studies of different scale (global, regional, and local) carried out at the Center for Imaging the Earth's Interior at the University of Colorado in collaboration with other seismological groups in US and abroad (Shapiro et al., 2005; Bensen et al., 2007, 2008, 2009; Lin et al., 2008, 2009, 2010; Moschetti et al., 2010a,b; Vilaseńor et al., 2007; Yang et al., 2007, Barmin et al., 2010). There are many other studies now (e.g., Yao et al., 2006; Li et al., 2009).
Physical backgrounds of this technique are shown in Figure 15. Data processing is explained in Figures 16-17 (Bensen et al., 2007).

Correlations of random wavefields

Random wavefield - sum of waves emitted by randomly distributed sources

Cross-correlation of waves emitted by a single source between two receivers

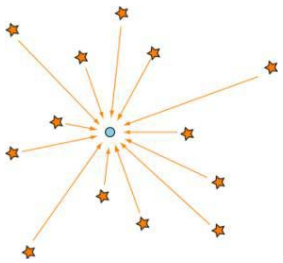

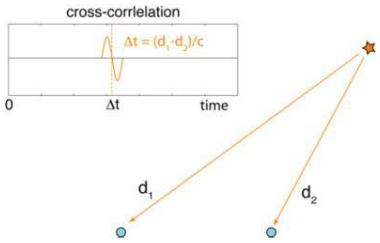

Correlations of random wavefields

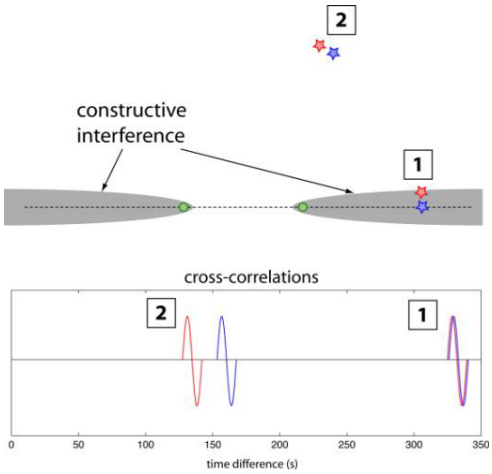

Sources are in constructive interference when respective travel time difference is similar

Effective density of sources is high in the vicinity of the line connecting two receivers

Cross-correlation extracts waves propagating along the line connecting two receivers

Sensitivity kernel collapses to an ellipse (approximately) with the recievers at the foci.

Figure 15: Physical background of ANT.

Data Processing Procedure

Phase 1. Pre-processing of single-station data.

- Remove instrument, mean, trend, band-pass filter, cut to 1-day.
- Time-domain normalization: desensitize to earthquakes & instrumental irregularities.
- Spectral "whitening".

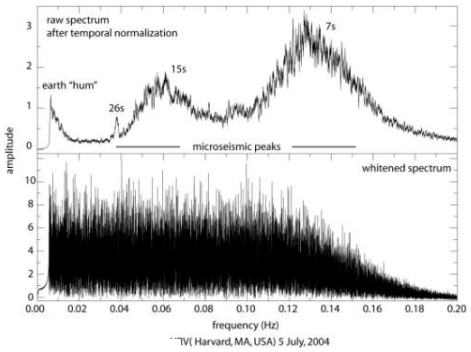

Data Processing Procedure

Phase 2. Processing on station-pairs: cross-correlation and stacking.

- Effect of temporal normalization.
- Effect of pre-whitening.

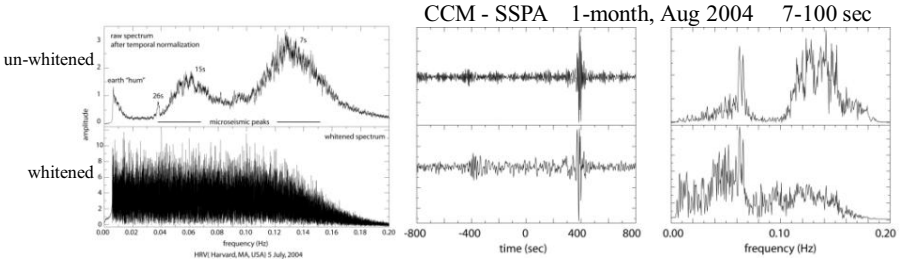

Figure 16: Data processing of ambient noise: normalization in frequency and time.

Data Processing Procedure

Phase 2. Processing on station-pairs: cross-correlation and stacking.

- Effect of temporal normalization.

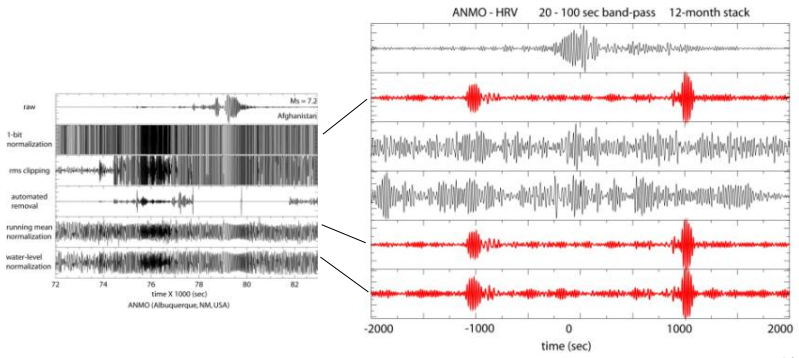

19

Data Processing Procedure

Phase 2. Processing on station-pairs: cross-correlation and stacking.

- Emergence of the signal with stacks of increasing length.

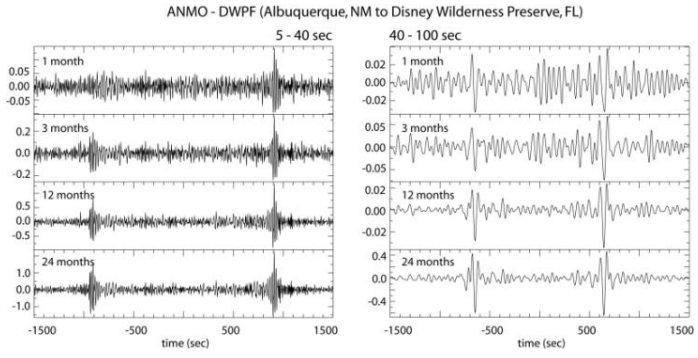

Figure 17: Data processing of ambient noise: effects of normalization in time and stacking.

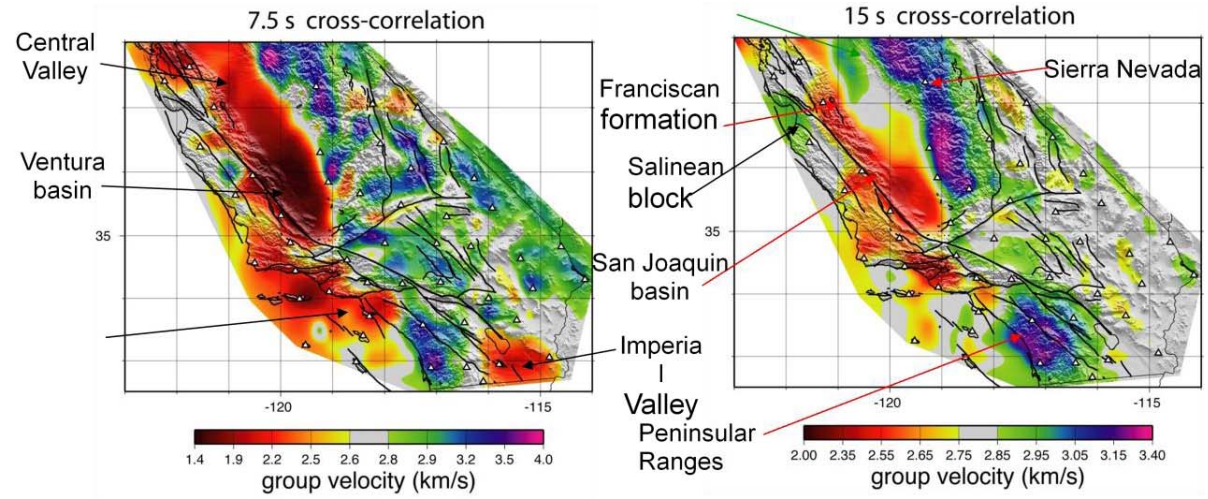

Figure 18: High resolution group velocity tomography of Californian crust from ambient noise.

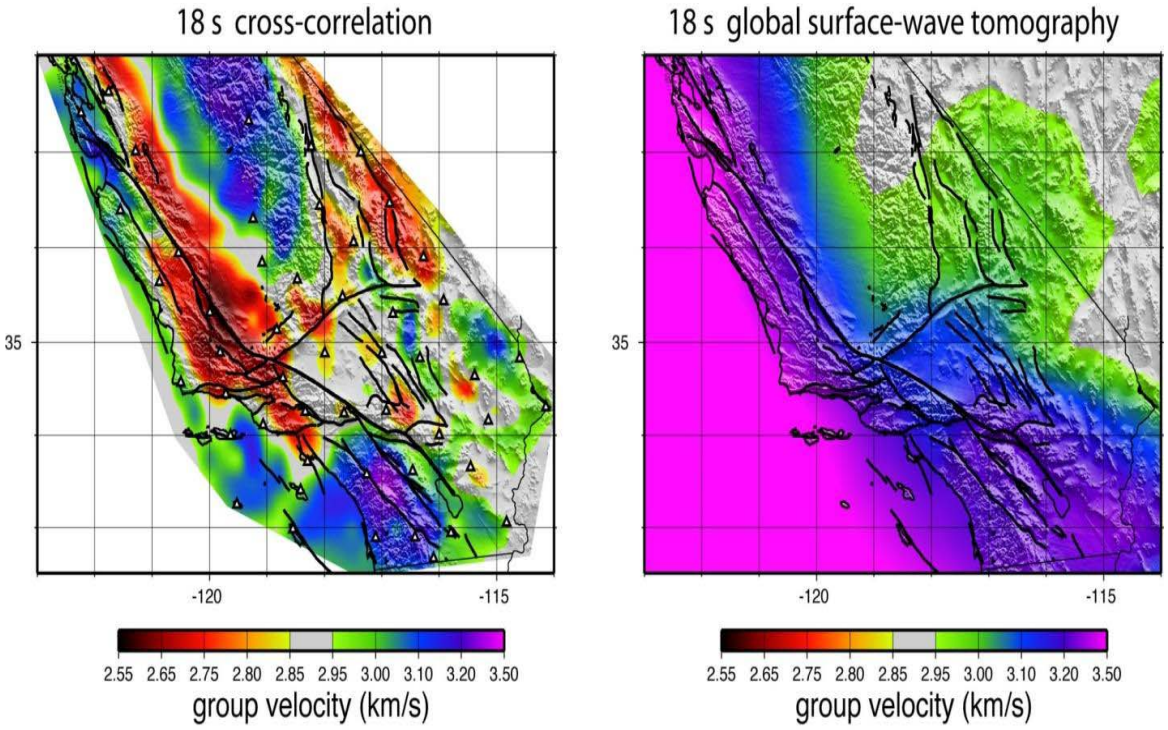

Figure 19: Comparison between traditional teleseismic group-velocity tomography and ANT.

Because short-period surface waves are mainly sensitive to shallow structure, they are very useful to constrain the structures of crust and uppermost mantle. In this study, we measure phase velocity dispersion curves from the ambient noise cross-correlations to obtain phase velocity tomographic maps at periods from 8 to 29 sec. Earlier, a two-plane-wave method considering

finite-frequency effects (Yang & Forsyth, 2006) was used to obtain Rayleigh-wave phase velocity maps at periods from 25 to 143 sec. We compare phase velocity maps at two overlapped periods 25 and 29 sec from the two methods, and find phase velocity is similar for both methods (Figure 20). The combined phase velocity data set from 8 to 143 sec is used to invert for 3-D Vs structure from the surface to ~200 km depth in the upper mantle beneath southern California.

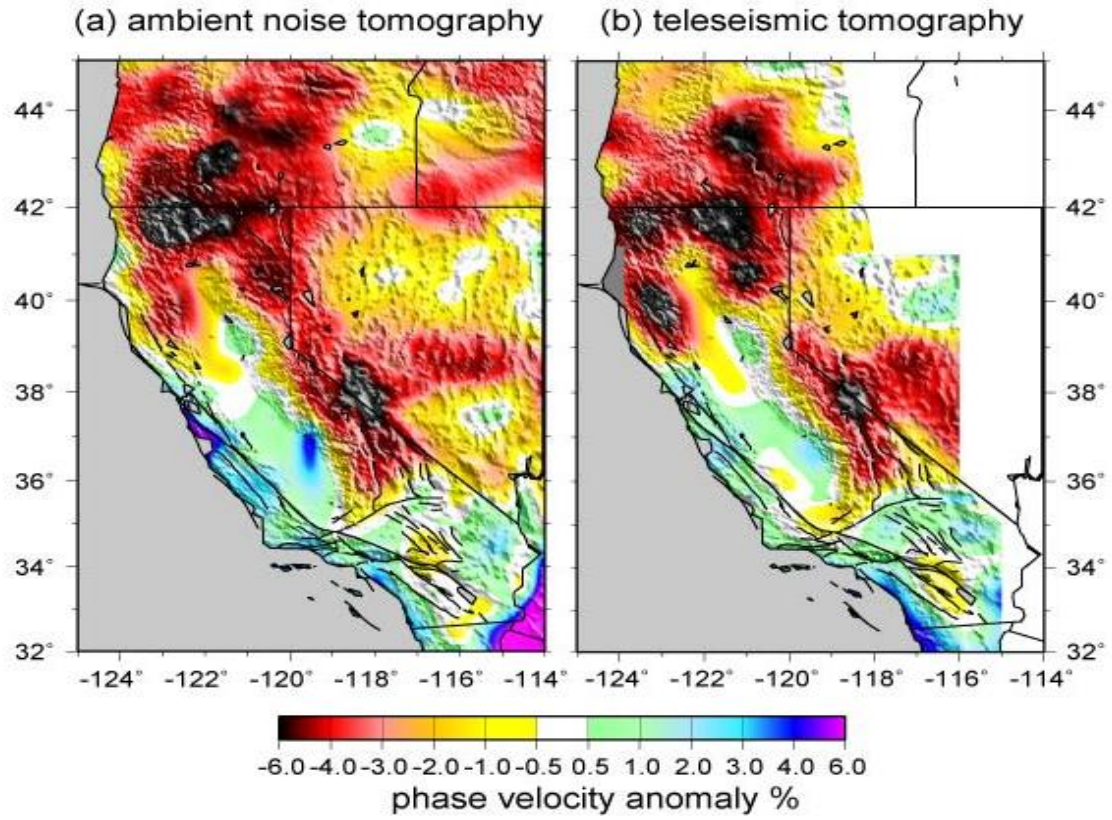

Figure 20. Phase velocity maps obtained by ANT and teleseismic tomography.

Ambient noise tomography of Europe was based on use of 12 months of VEBSN data across Europe for 2004. Data processing was followed by tomography to produce dispersion maps for 8-50 sec periods (Fgure 21).

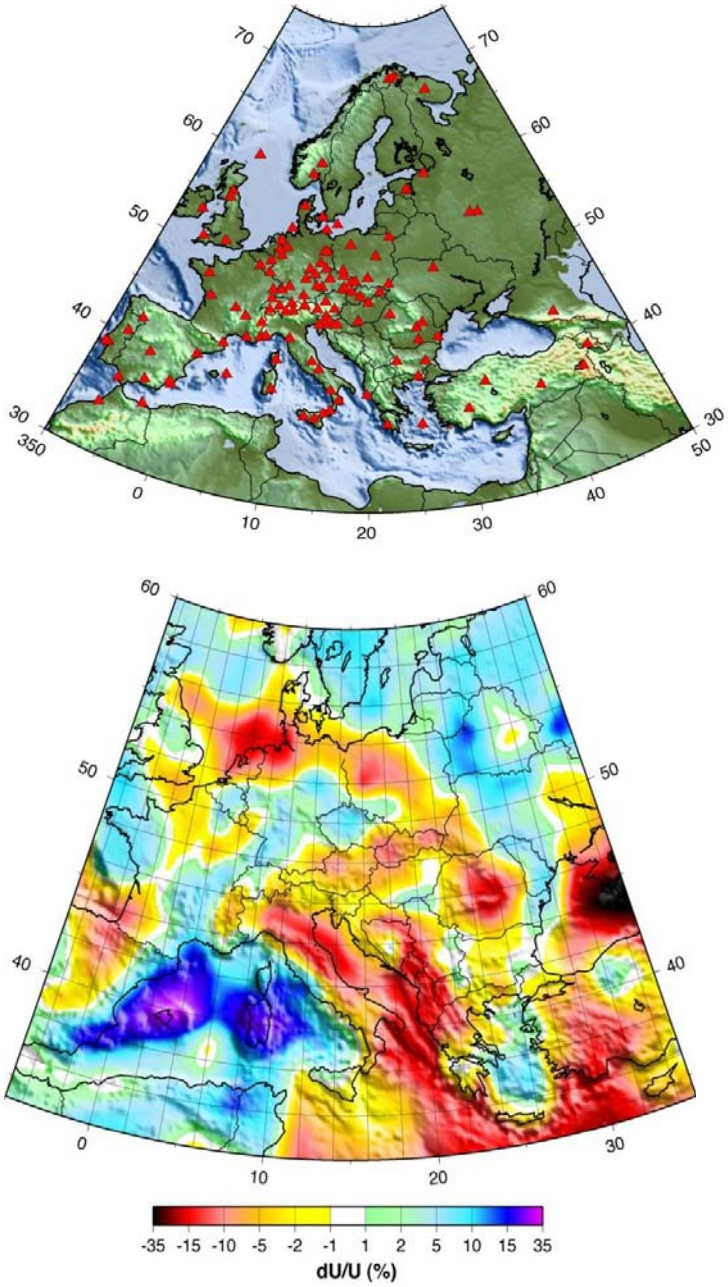

Figure 21: ANT of Europe; 20s Rayleigh-wave group velocity map from 3057 paths.

We have obtained group velocity maps of short period Rayleigh waves from 10 to 20 seconds for the Iberian Peninsula by cross-correlating 4 months of ambient noise data recorded by 40 permanent broadband stations in the region. Group velocity maps accurately image the main structural elements of the Iberian upper crust, including the Iberian Massif (the stable Hercynian core), Alpine orogens and major sedimentary basins. The Pyrenees and the Iberian cordillera are imaged as relatively high group velocities, in contrast with the Betic cordillera, which is characterized by low velocities (Figure 22)

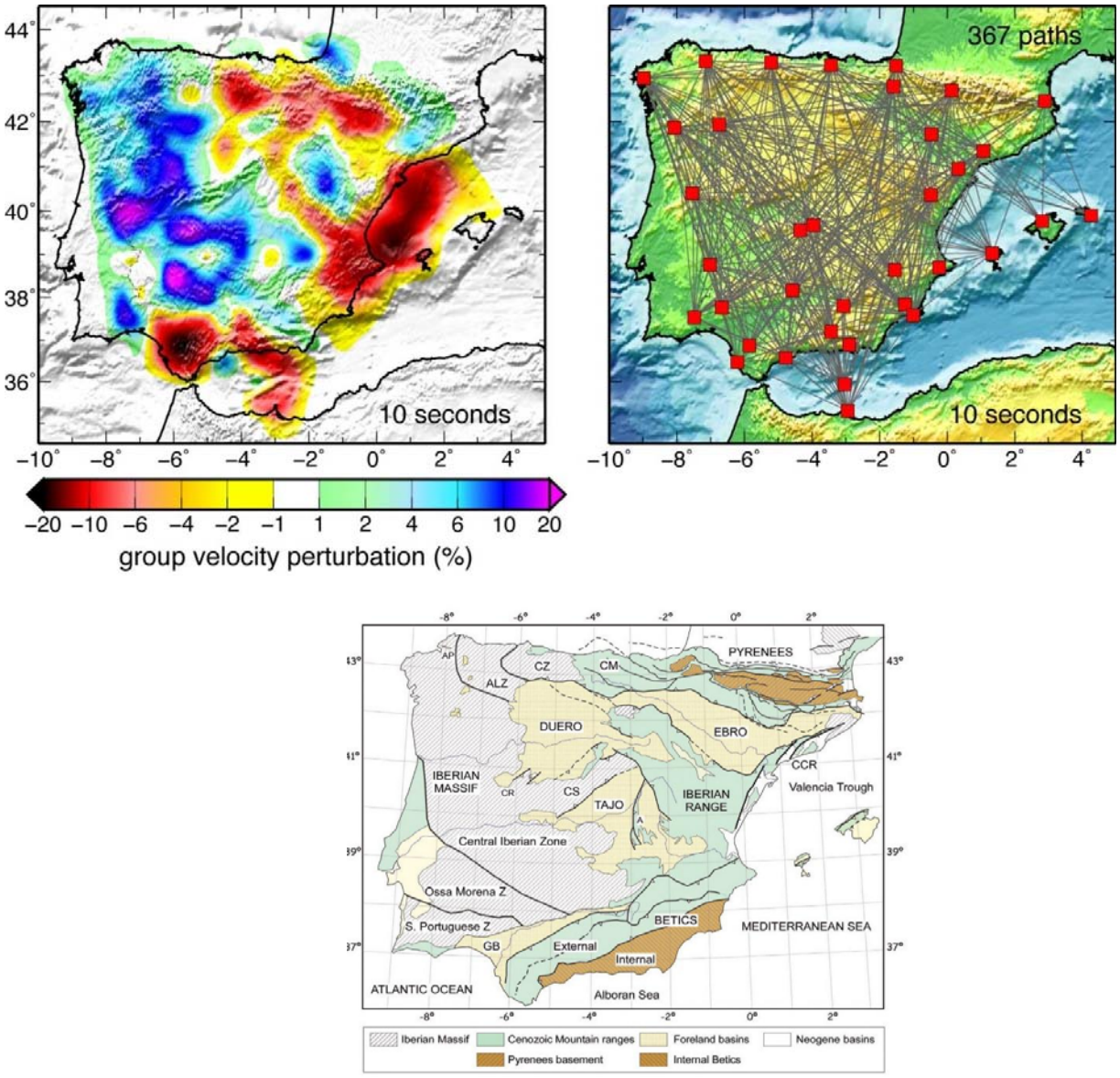

Figure 22. Ambient Noise Tomography in Spain, 10s Rayleigh-wave group velocity map.

We present the first New Zealand-wide study of surface wave dispersion using ambient noise observed at 42 broadband stations in the national seismic network (GeoNet) and the Global Seismic Network (GSN). After selecting the highest quality dispersion curve measurements, we compute group velocity maps at 7--25 s periods. These maps, and 1--D shear wave velocity models, exhibit clear correlations with major geological structures (Figure 23).

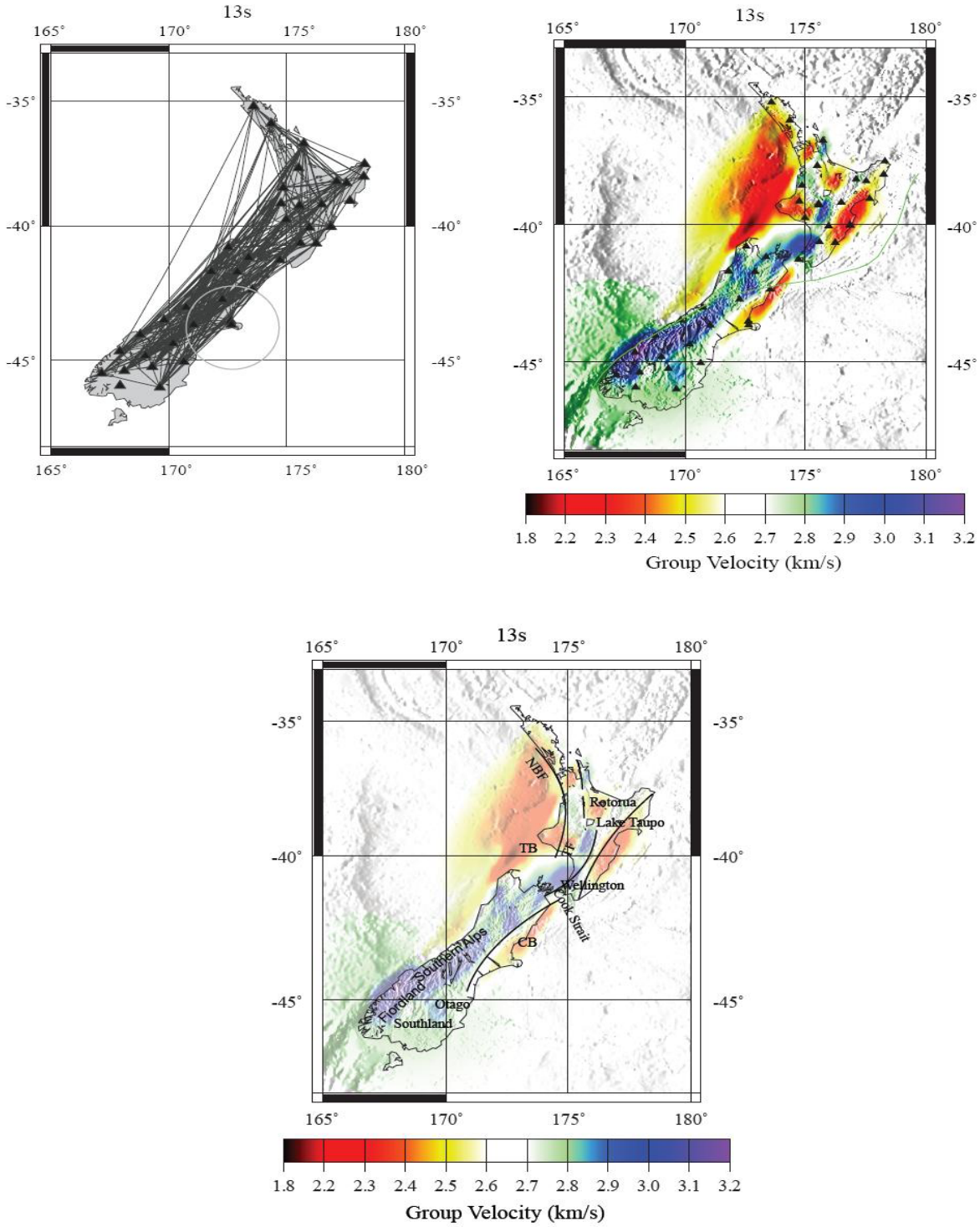

Figure 23: Ambient noise tomography of New Zealand

Phase velocity tomography using eikonal equation (Lin et al., 2009)

The traditional approach to seismic tomography begins with a statement of the forward problem that links unknown earth functional (such as seismic wave speeds, surface wave phase or group speeds, etc.) with observations. The nontraditional (eikonal) approach is based on the following approximate relation which is derived from the Helmholtz equation:

$$\frac{\kappa}{c_i(r)} \cong \nabla \tau(r_i, r)$$

Here τ ($\boldsymbol{r_i}$, $\boldsymbol{r}$) are phase trave time surfaces for positions $\boldsymbol{r}$ relative to an effective source located at $\boldsymbol{r_i}$ which are considered known, c_i is the phase speed and $\boldsymbol{k}$ is the unit wavenumber vector for traveltime surface i at position $\boldsymbol{r}$.

In this case, the magnitude of the gradient of the phase travel time is simply related to the 'local' phase slowness at $\boldsymbol{r}$ and the direction of the gradient provides the 'local' direction of propagation of the wave. Thus, the eikonal equation places local constraints on the surface wave speed.

The approximation above is justified either at high frequencies or if the spatial variation of the amplitude field is small compared with the gradient of the travel time surface. The latter is the less restrictive constraint and will hold if lateral phase speed variations are sufficiently smooth to produce a relatively smooth amplitude field. Moreover, when repeated measurements are performed with phase travel time surfaces from different effective sources, the errors caused by this approximation are likely to interfere destructively, but will contribute to the estimated uncertainty especially when the wavelength is shorter than the length scale of the velocity structure.

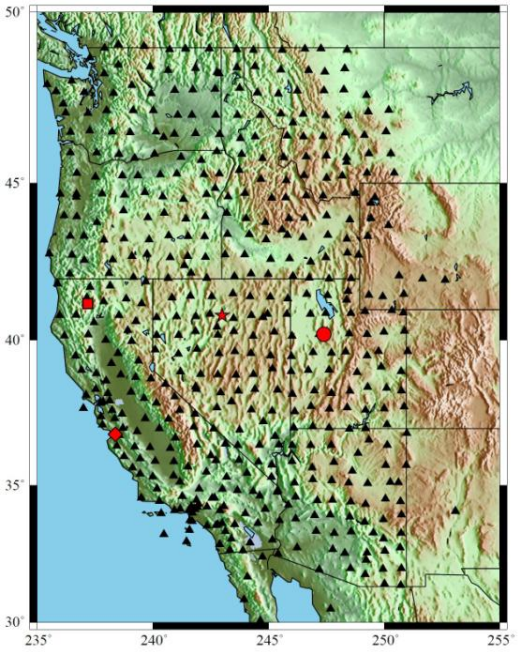

Figure 24: The 499 stations are identified by black triangles. Most stations are from the EarthScope/USArray Transportable Array (TA), but a few exceptions exist, such as NARS Array stations in Mexico.

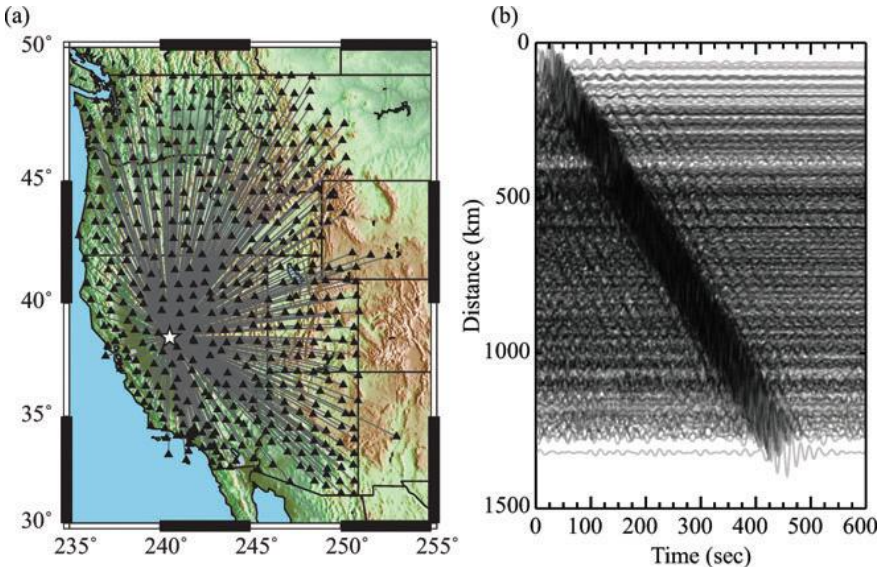

Figure 25: (a) Great circle paths linking station R06C (southeast of Lake Tahoe, identified by the white star) with all TA stations where cross-correlations were obtained. (b) Symmetric component record section for 15–30 s period band-passed vertical–vertical cross-correlations with station R06C in common. More than 450 cross-correlations are shown. Clear move-out near 3 km/s is observed.

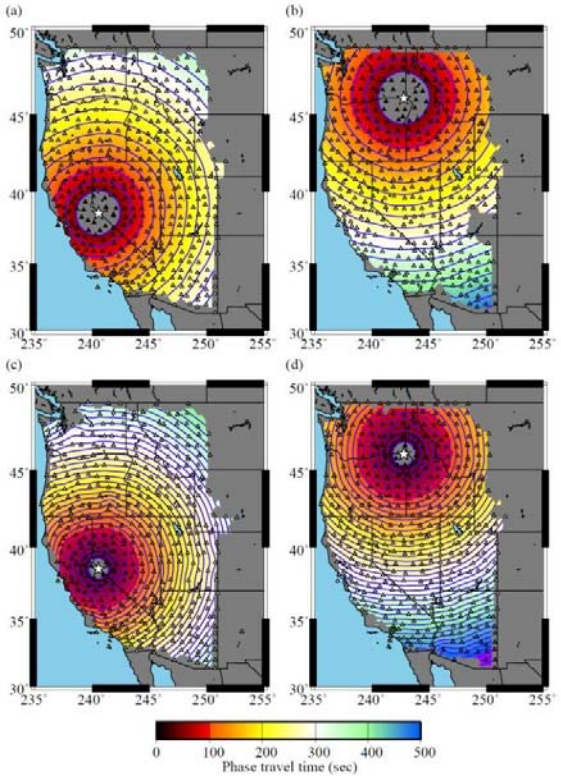

Figure 26: Rayleigh wave phase speed travel time surfaces at periods of (a, b) 24 s and (c, d) 12 s centered on two 'effective sources': stations R06C (eastern California) and F10A (northeastern Oregon). Travel time level lines are presented in increments of the wave period.

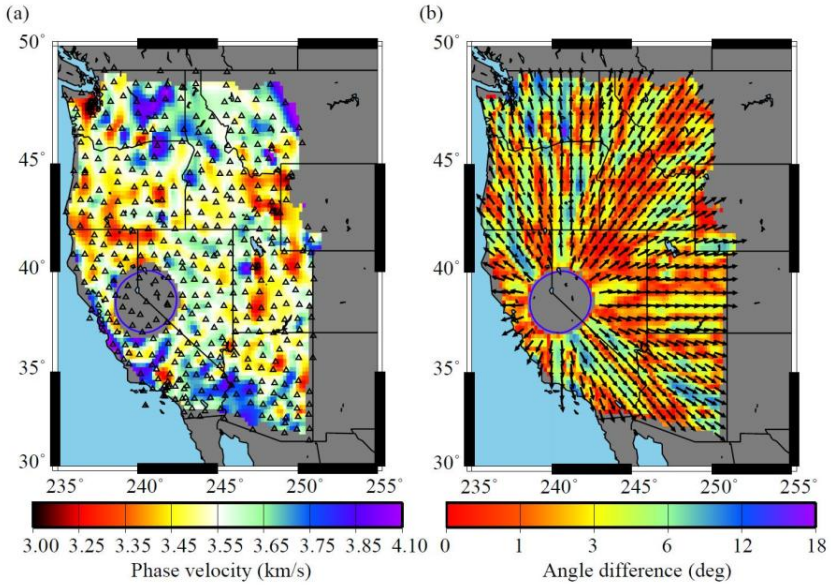

Figure 27: (a) The phase speed inferred from the eikonal equation for the 24 s Rayleigh wave travel time surface shown in Fig. 26 centered on station R06A. (b) The propagation direction determined from the gradient of the phase travel time surface at each point is shown with arrows. The difference between the observed propagation direction and the straight-ray prediction (radially away from stations R06A) is shown as the background color.

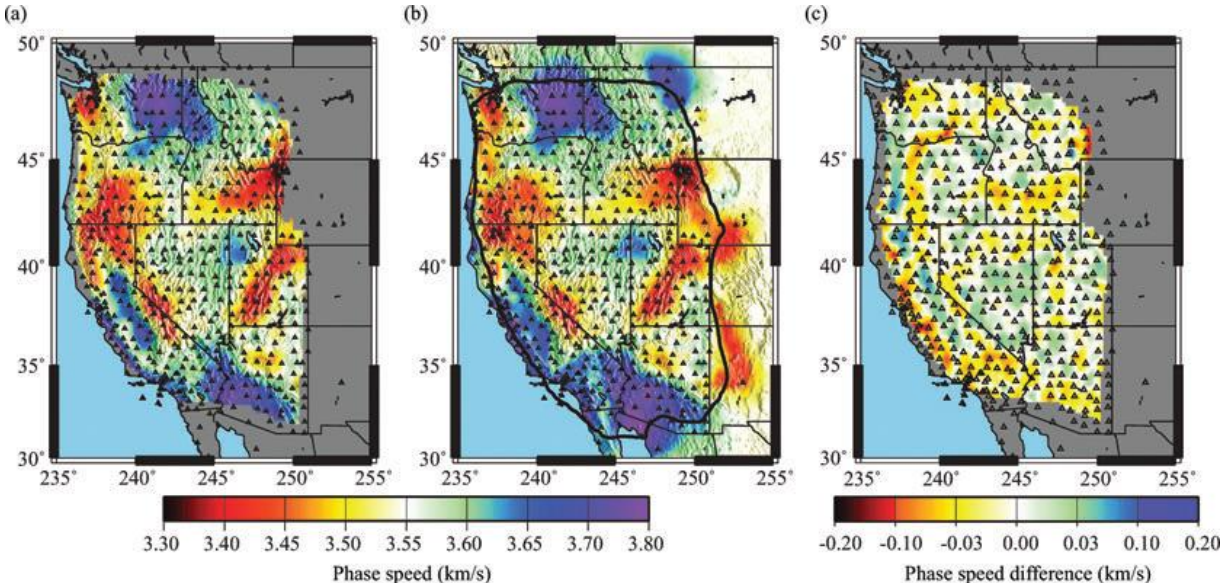

Figure 28: (a) The 24 s Rayleigh wave isotropic phase speed map derived from eikonal tomography. The isotropic phase speed at each point is calculated from the distribution of local phase speeds determined from each of the phase travel time maps. (b) Same as (a), but the straight-ray inversion of Barmin *et al.* (2001) is used. The black line is the 100 km resolution contour. (c) The difference between eikonal and straight-ray tomography is shown where positive values indicate that the eikonal tomography gives a higher local phase speed.

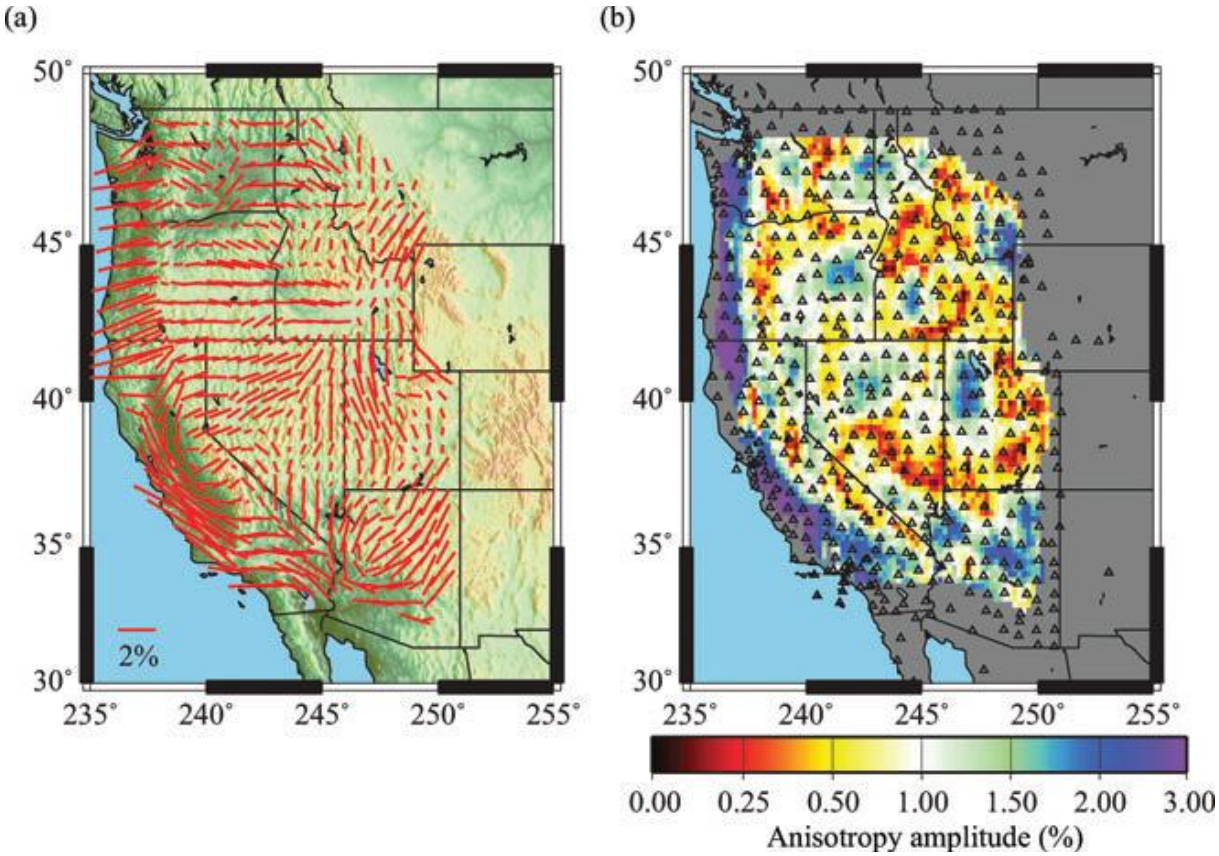

Figure 29: (a) The 24 s period Rayleigh wave azimuthal anisotropy fast axis directions and peak-to-peak amplitudes, $2A/c_0$, which are proportional to the length of the bars. (b) Peak-to-peak amplitude of anisotropy presented in percent.

Epicenter Location Using Ambient Seismic Noise

The purpose of this research is to improve seismic event location accuracy and event characterization by exploiting Empirical Green's Functions (EGFs) that emerge by cross-correlating long time sequences of ambient noise observed at pairs of seismic stations. Because ambient noise EGFs are dominated by surface waves, the method uses surface wave energy for location purposes. Present efforts apply Rayleigh wave EGFs from 5 to 15 sec period to the epicentral location problem. The method of epicentral location as well as proof-of-concept applications for a series of seismic events in the western US are described in Ritzwoller et al. (2010).

The main features of our method as it exists now are:

1a) We assume that inside of "the region of interest" where seismic events may occur, a temporary dense local array, termed the **base stations**, is deployed. Second, there is a more

distant permanent (but potentially sparse) regional network of stations termed the **remote stations** (Figure 30). Using what are now well established methods (e.g., Bensen et al. (2007)), the EGFs from every base to every remote station are computed. At this stage of the project, we use only vertical-to-vertical components of EGFs here, which are dominated by Rayleigh waves.

1b) The amplitude spectra of EGFs and signals recorded at remote stations are equalized without changing its phase spectrum. This is done by replacing the amplitude spectrum of the event record with the amplitude spectrum of the EGF, or by replacing both the EGF and event record's amplitude spectra with the square root of the product of the amplitude spectra of the event and the EGF.

1c) The set of these EGFs is transformed by means of a frequency-time analysis (FTAN) as described by Levshin et al.(1971, 1980) into two-dimensional (frequency-time) representations of signal power in a certain range of periods and group velocity times corresponding to the fundamental mode of Rayleigh wave in a continental crust. Typically, we select period range 5-15 s and group velocity range 2.5-4.5 km/s.

1d) We cover the "region of interest" by the grid of points which spacing depends on density of base stations' array. For each grid points we are able to calculate so-called **Composite EGFs (CEGFs)** (Figure 31) by transforming and stacking the individual EGFs for a given remote station. The transformation is done by rescaling FTAN-diagrams in time according to the distance between a grid point and a remote station. At this stage of the method's development we assume that group velocity in the selected period range does not depend on frequency, and do not use the phase velocity information provided by FTAN.

1e) The same transformation is applied to the signals recorded by all remote stations. Now for each grid point and each remote station (Figure 32a,b) we have a FTAN-diagram of CGF and FTAN-diagram of the signal. Example of such couple of diagrams is shown in Figure 32c,d.

1f) The next step is cross-correlation in a time domain of two types of FTAN-diagram: from records of all remotes stations and CEGFs for all points of the grid. The time delays of the maximum amplitudes of cross-correlation functions (Figure 32e) are found and used to construct the quadratic functional of residuals similar to one used in body wave hypocenter location. The grid point with a minimal value of this functional is considered as an epicenter, and average value of residuals at this point provides an estimate of the origin time.

1g) Confidence ellipse for the position of epicenter is constructed following Flinn (1965). Several examples of application of this technique for location of virtual and real seismic events are shown in figures 33-35.

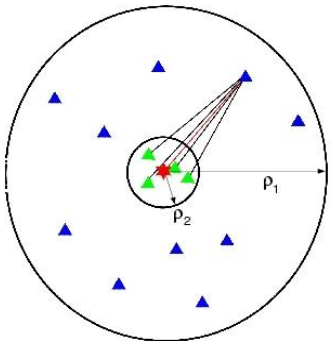

Figure 30: Schematic observational setting. A relatively dense set of temporary "base stations" (green triangles) encompasses the source region of interest (event is denoted by the red star). A sparse set of permanent "remote stations" (blue triangles) lie farther from the region of interest.

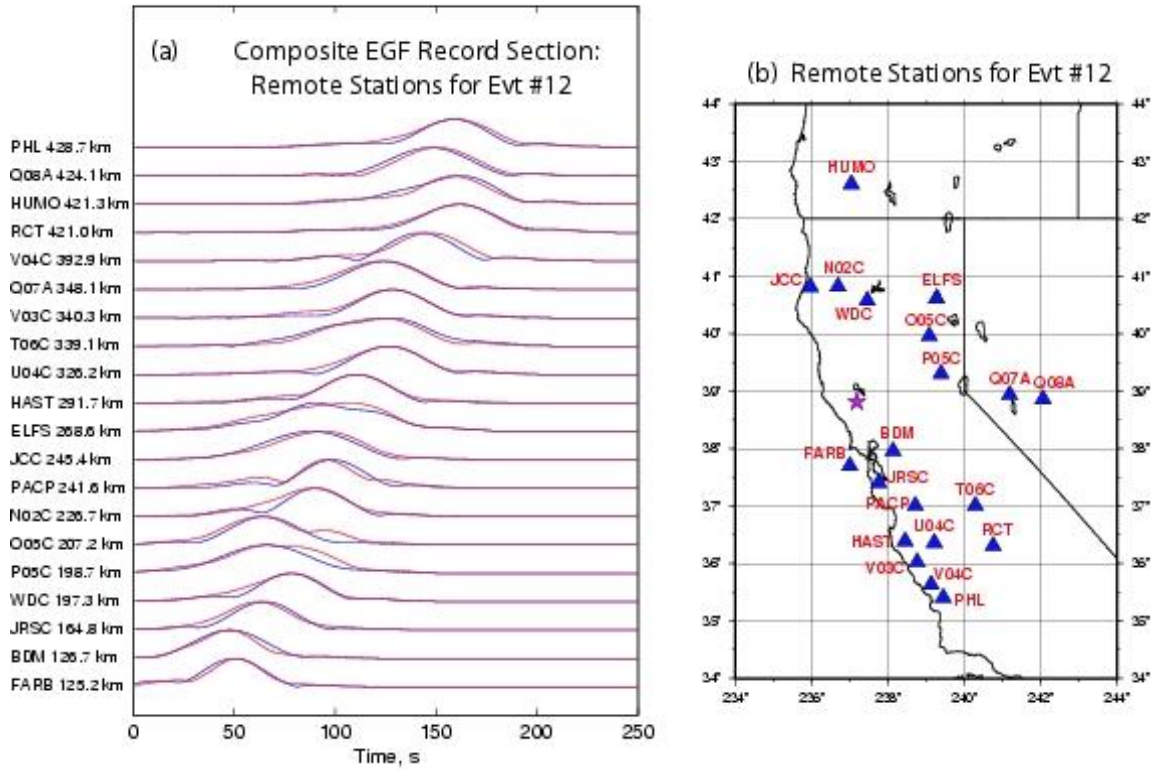

Figure 31: Record section of the Composite Empirical Green's Functions compared with the earthquake records at 20 remote stations for Event #12. (a) Envelope functions of the earthquake observed at the remote stations (red lines) are compared with envelopes of the Composite EGFs (blue lines). Band-pass: 7-15 sec period. Epicentral distances and station names are indicated at left. (b) Locations of the remote stations and the earthquake.

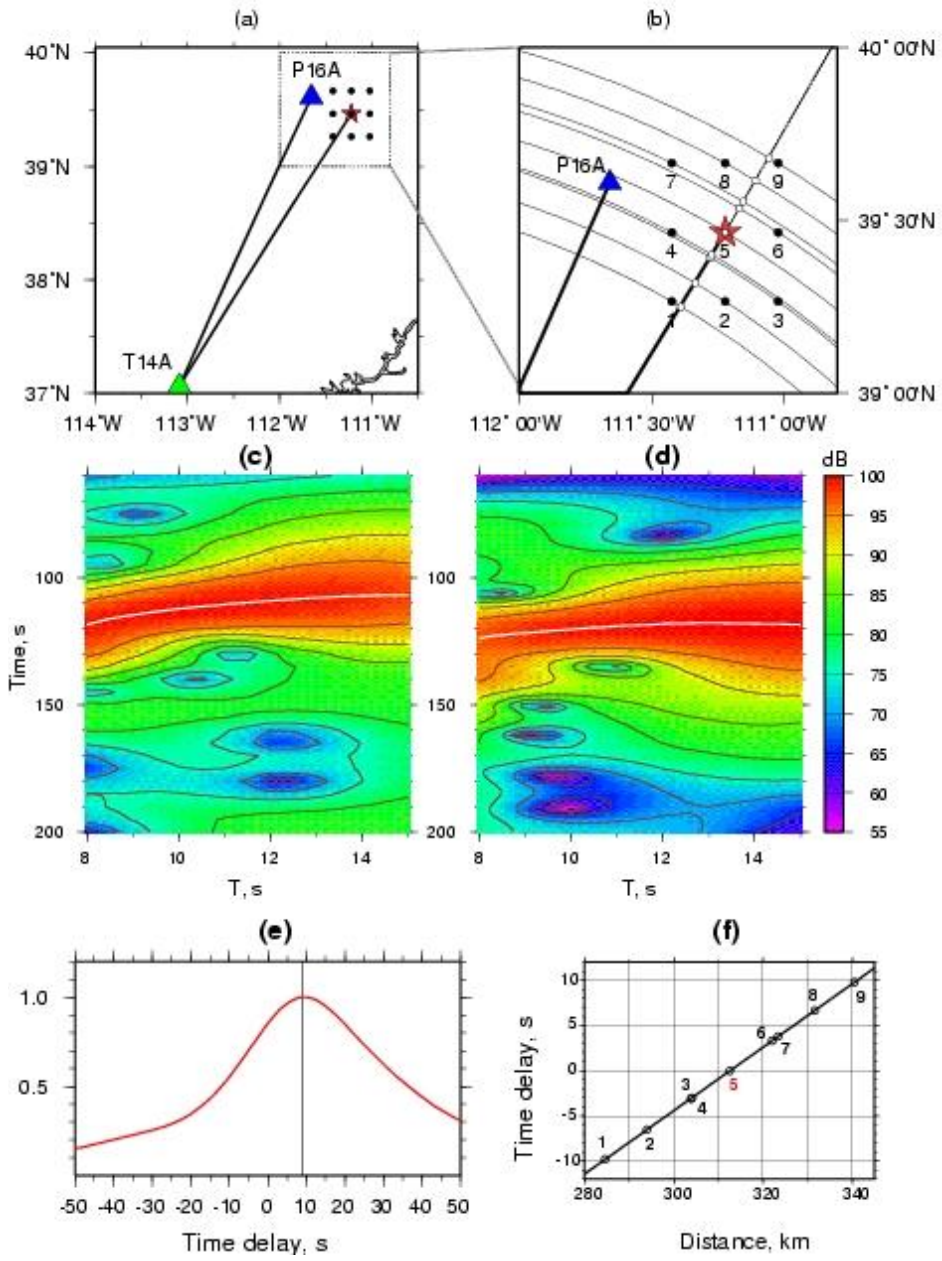

Figure 32: Illustration of location procedure based on cross-correlation of frequency-time (FT) representations of an event record and an EGF. (a) Event-station geometry. (b) FT-diagram of the CEGF for the same station and the same grid point. (c) Cross-correlogram of the two FT-representations in (a) and (b) with the time delay of the maximum around 10 s.

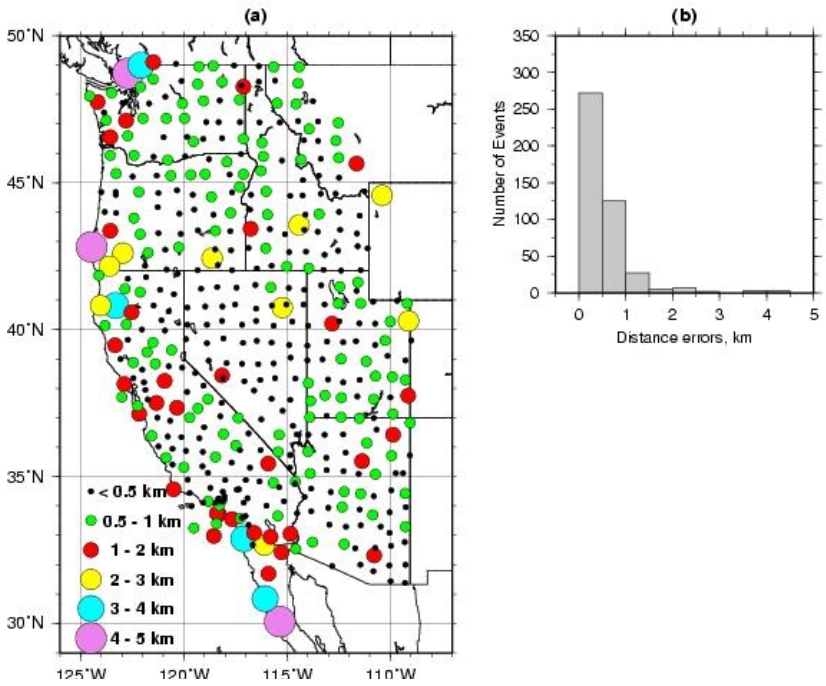

Figure 33: Location errors of 445 ”virtual sources" (stations) in California and surrounding states. (a) Map of location errors for the stations. The distance between the known station location and the estimated location, in km, for each station position is shown by the colored circles. (b) Histogram of location errors (in km).

Figure 34: Schema of the Crandall Canyon min and location of mine collapse. Our location of the event (green star) and corresponding 90% confidence ellipse. The left yellow push-pin marks the USGS event location, and the right push-pin is the approximate location of the mine collapse and trapped miners.

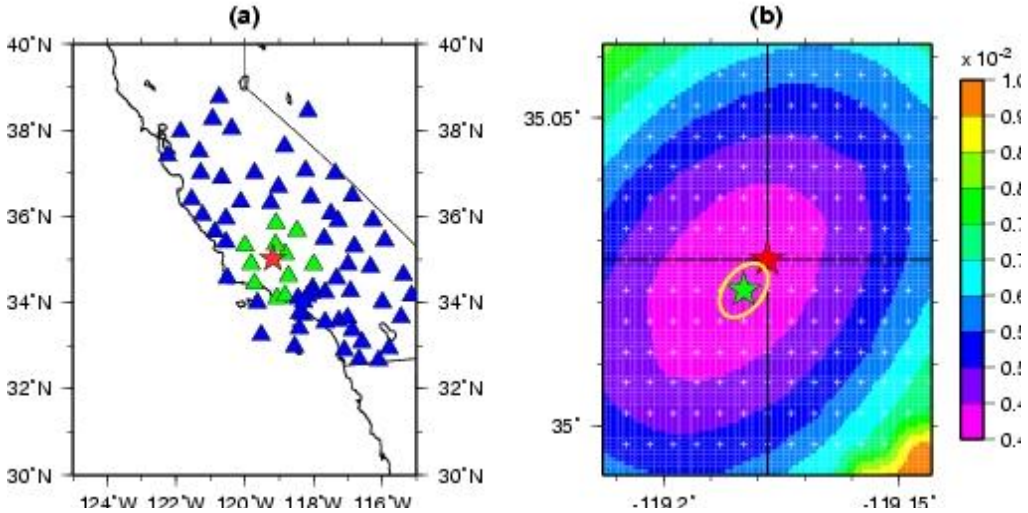

Figure 35: California event #1 station configuration and misfit surface. (a) Symbols: base stations (green triangles), remote stations (blue triangles), and event location (red star). (b) Map of residuals: our event location (green star), USGS location (red star), 90% confidence ellipsoid (yellow line). Grid points are marked with white crosses and are separated by about 500 m.

REFERENCES

Barmin, M.P., Levshin, A.L., & Ritzwoller, M.H., 2001. A fast and reliable method for surface wave tomography, *Pure and Appl. Geoph*., 158, n.8, 1351-1375.

Barmin, M.P., Levshin, A.L. & Ritzwoller, M.H., 2005. Finite-frequency group velocity kernels for surface wave tomography, *EOS, Trans. Am. geophys. Un.* , 86(52), Fall Meet. Suppl., Abstract S51E-1057.

Barmin, M.P., A.L. Levshin, Y. Yang, and M.H. Ritzwoller, 2010. Epicentral location based on Rayleigh wave empirical Green's functions from ambient seismic noise, *Geophys. J. Int.*, submitted.

Bensen, G. D., M. H. Ritzwoller, M. P. Barmin, A. L. Levshin, F. Lin, M. P. Moschetti, N. M. Shapiro, and Y. Yang, 2007. Processing seismic ambient noise data to obtain reliable broad-band surface wave dispersion measurements, *Geophys. J. Int*., 169(3), 1239-1260, DOI: 10.1111/j.1365-246X.2007.03374.x.

Bensen, G.D., M.H. Ritzwoller, and N.M. Shapiro, 2008. Broad-band ambient noise surface wave tomography across the United States, *J. Geophys. Res.*, 113, B05306, 21 pages, doi:10.1029/2007JB005248.

Bensen, G.D., M.H. Ritzwoller, and Y. Yang, 2009. A 3D shear velocity model of the crust and uppermost mantle beneath the United States from ambient seismic noise, *Geophys. J. Int.*, 177(3), 1177-1196.

Dahlen, F.A. & Tromp, J., 1998. *Theoretical Global Seismology*, Princeton University Press, Princeton, New Jersey.

Dahlen, F.A. and Y. Zhou, 2006. Surface-wave group-delay and attenuation kernels, *Geophys. J. Int.*, 65, 545-554.

Dziewonski, A.M. & Anderson, D.L., 1981. Preliminary reference Earth model, *Phys. Earth. Planet. Inter*., 25, 297-356.

Engdahl, E. R., R. van der Hilst, and R. Buland, 1998. Global teleseismic earthquake relocation with improved travel time and procedures for depth determination, *Bull. Seismol. Soc. Am*., 88, 722 - 743.

Flinn, E.A. ,1965. Confidence regions and error determinations for seismic event locations. *Rev. Geophys*.,3,pp.157-185.

Kennett, B.L.N., Engdahl, E.R., & Buland, R., 1995. Constraints on seismic velocities in the Earth from travel times, *Geophys. J. Intl'*, 122, 403-416.

Levshin, A.L., Yanovskaya, T.B., Lander, A.V., Bukchin, B.G., Barmin, M.P., Ratnikova, L.I., & Its, E.N., 1989. Recording, identification, and measurement of surface wave parameters. In: *Seismic surface waves in a laterally inhomogeneous Earth* (Keilis-Borok, V.I., editor). Kluwer Academic Publisher, Dordrecht, 131-182.

Levshin,A.L., M.H. Ritzwoller, and J.S. Resovsky, 1999. Source effects on surface wave group travel times and group velocity maps*, Phys. Earth Planet. Inter*.,115, pp.293-312.

Levshin, A.L., Ritzwoller, M.H., Barmin, M.P., & Villaseńor, A., 2001. New constraints on the Arctic crust and uppermost mantle: Surface wave group velocities, Pn, and Sn, *Phys. Earth. Planet. Inter*., 123, 185-204.

Levshin, A.L., and M.H. Ritzwoller, 2002. Application of a global-scale 3D Model to improve regional locations, *Studia Geoph. et Geod*., 46, 2, 289-292.

Levshin, A.L., M.P. Barmin, M.H. Ritzwoller, and J. Trampert, 2005a. Minor-arc and major-arc global surface wave diffraction tomography, *Phys. Earth Planet. Int*., 149, 205-223.

Levshin, A.L., M.H. Ritzwoller, and N.M. Shapiro, 2005b. The use of crustal higher modes to constrain crustal structure across Central Asia, *Geophys. J. Int*., 160, 961-972, 2005.

Levshin, A.L., and G.F. Panza. 2006. Caveats in modal inversion of seismic surface wave_fields, *Pure and App. Geophys.*, 163 (7).

Levshin, A.L., J. Schweitzer, C. Weidle, N. Shapiro, and M. Ritzwoller, 2007. Surface wave tomography of the Barents Sea and surrounding regions, *Geophys. J. Int.,* 170, p. 441-459, doi:10.1111/j.1365-246X.2006.03285.x.

Levshin, A.L., X. Yang, M.P. Barmin, and M.H. Ritzwoller, 2010. Midperiod Rayleigh wave attenuation model for Asia, *Geochem., Geophys., Geosyst.*, in press.

Li H., W. Su, C.-Y. Wang, and Z. Huang, 2009. Ambient noise Rayleigh wave tomography in western Sichuan and eastern Tibet. *Earth and Planet. Sci. Lett*., 282,1-4,201-211.

Lin, F., M.P. Moschetti,and M.H. Ritzwoller, 2008. Surface wave tomography of the western United States from ambient seismic noise: Rayleigh and Love wave phase velocity maps, *Geophys. J. Int.*, 173(1), pp. 281-298, doi:10.1111/j1365-246X.2008.03720.x.

Lin, F.-C., M.H. Ritzwoller, and R. Snieder, 2009. Eikonal tomography: surface wave tomography by phase-front tracking across a regional broad-band seismic array, *Geophys. J. Int.*, 177(3), 1091-1110.

Lin, F.C., M.H. Ritzwoller, Y. Yang, M.P. Moschetti, and M.J. Fouch, 2010. The stratification of seismic azimuthal anisotropy in the western US, *Nature Geoscience*, submitted.

Lin, F.C. and M.H. Ritzwoller, 2010. Empirically determined finite frequency sensitivity kernels for surface waves, *Geophys. J. Int.*, doi: 10.1111/j.1365-246X.2010.04643.x.

Mitchell, B.J., 1984. On the inversion of Love- and Rayleigh-wave dispersion and implications for the Earth structure and anisotropy, *Geophys. J. R. astr. Soc*., 76, 233-241.

Montagner, J.-P. & Jobert, N., 1988. Vectorial tomography. II: Application to the Indian Ocean, *Geophys. J. R. astr. Soc*., 94, 309-344.

Montagner, J.-P. & Anderson, D.L., 1989. Constrained reference mantle model, Phys. *Earth. Planet. Inter*. 58, 205-227.

Montagner, J.-P. & Tanimoto, T., 1991. Global upper mantle tomography of seismic velocities and anisotropies, *J. Geophys. Re*s., 96, 20,337-30,351.

Montagner, J.-P., 1994. Can seismology tell us anything about convection in the mantle?, *Rev. Geoph*. 32, 115-137.

Montagner, J.-P., 1998. Where can seismic anisotropy be observed in the Earth's mantle? In boundary layers ..., *Pure and Appl. Geoph*., 151, 223-256.

Moschetti, M.P., M.H. Ritzwoller, and N.M. Shapiro, 2007. Surface wave tomography of the western United States from ambient seismic noise: Rayleigh wave group velocity maps, *Geochem., Geophys., Geosys.*, 8, Q08010, doi:10.1029/2007GC001655.

Moschetti, M.P., M.H. Ritzwoller, F.C. Lin, and Y. Yang, 2010a. Crustal shear velocity structure of the western US inferred from amient noise and earthquake data, *J. Geophys. Res.*, submitted.

Moschetti, M.P., M.H. Ritzwoller, and F.C. Lin, 2010b. Seismic evidence for widespread crustal deformation caused by extension in the western USA, *Nature*, 464, Number 7290, 885-889.

Nataf, H.-C., Nakanishi, I., & Anderson, D.L., 1986. Measurements of mantle wave velocities and inversion for lateral heterogeneities an anisotropy, *J. Geophys. Res., 91*, 7261-7307.

Nolet, G., 1990. Partitioned wave-form inversion and 2-dimensional structure under the network of autonomously recording seismographs, *J. Geophys. Res*., 95, 8499-8512.

Nolet, G. *A Breviary of Seismic Tomography*, 2008. Cambridge University Press.

Pechmann, J.C., W.I. Arabasz, K.L. Pankow, R. Burlacu,and M.K. McCarter, 2007. Seismological report on the 6 Aug 2007 Crandall Canyon Mine Collapse in Utah, *Seismol. Res. Lett.*, 79, 5, pp. 620-636.

Ritzwoller, M.H. & Levshin, A.L.,1998. Eurasian surface wave tomography: group velocities, *J. Geophys. Res.*, 103, 4839-4878.

Ritzwoller, M.H., Levshin, A.L., Ratnikova, L.I., & Egorkin, A.A., 1998. Intermediate period group velocity maps across Central Asia, Western China and parts of Middle East, *Geophys. J. Intl*., 134, 315-328.

Ritzwoller, M.H., Shapiro, N.M., Levshin, A.L., & Garret, M.L., 2001 Crustal and upper mantle structure beneath Antarctica and surrounding oceans, *J. Geophys. Res*., 106, 30645-30670.

Ritzwoller, M.H., N.M. Shapiro, M.P. Barmin, and A.L. Levshin, 2002a. Global surface wave diffraction tomography, *J. Geophys. Res*.,107(B12), 2335, doi:10.1029/2002JB001777.

Ritzwoller, M.H., N.M. Shapiro, A.L. Levshin, E.A. Bergman, E.A. Engdahl, 2003. The ability of global models to locate regional events, *J. Geoph. Res.*, 108(B7), 2353, doi:10.1029/2002JB00.

Ritzwoller, M.H., Ambient noise seismic imaging, *McGraw Hill Yearbook of Science and Technology 2009.*

Shapiro, N.M. and M.H. Ritzwoller, 2002. Monte Carlo inversion for a global shear velocity model of the crust and upper mantle, *Geophys. J. Int.*, 151, 88-105.

Shapiro, N.M. M. Campillo, L. Stehly, and M.H. Ritzwoller, 2005. High resolution surface wave tomography from ambient seismic noise, *Science*, 307(5715), 1615-1618.

Smith, M.L. & Dahlen, F.A., 1973. The azimuthal dependence of Love- and Rayleigh-wave propagation in a slightly anisotropic medium*, J. Geophys. Res.*, 78, 3321-3333.

Snieder, R., 2004. Extracting the Green's function from the correlation of coda waves: a derivation based on stationary phase, *Phys. Rev. E,* **69,** 046610.

Spetzler, J., Trampert, J., & Snieder, R., 2001. Are we exceeding the limits of the great circle approximation in global surface wave tomography? *Geoph. Res. Let.*, 28, 2341-2344.

Sun, X., X. Song, S. Zheng, Y. Yang, M. Ritzwoller, 2010. Three dimensional shear velocity structure of crust and upper mantle in China from ambient noise surface wave tomography, *Earthquake Science*, submitted.

Trampert, J. & Woodhouse, J.H., 1995. Global phase velocity maps of Love and Rayleigh waves between 40 and 150 s period, *Geophys. J. Intl'*, 122, 675-690.

Trampert J. and J. Spetzler, 2006. Surface wave tomography: Finite-frequency effects lost in the null space, *Geophys. J. Int.*, 164, 394-400.

Villaseńor, A., Ritzwoller, M.H., Levshin, A.L., Barmin, M.P., Engdahl, E.R., Spakman, W., & Trampert, J., 2001. Shear velocity structure of Central Eurasia from inversion of surface wave velocities, *Phys. Earth. Planet. Inter*., 123, 169-184.

Villaseńor, A., Y. Yang, M.H. Ritzwoller, and J. Gallart, 2007. Ambient noise surface wave tomography of the Iberian Peninsula: Implications for shallow seismic structure, *Geophys. Res. Lett.*, 34, L11304, doi:10.1029/2007GL030164.

Weaver, R.L. and O.I. Lobkis, 2001. Ultrasonics without a Source: Thermal Fluctuation Correlations at MHz Frequencies, *Phys. Rev. Lett*., 87, paper 134301..

Woodhouse, J.H., 1988. The calculation of the eigenfrequencies and eigenfunctions of the free oscillations of the Earth and the Sun, in: *Seismological Algorithms* (D. J. Doornbos, ed.), 321-370.

Woodhouse, J.H. & Dziewonski, A.M., 1984. Mapping the upper mantle: three dimensional modeling of Earth's structure by inversion of seismic waveforms, *J. Geophys. Res.*, 89, 5953-5986.

Yang, X., S.R. Taylor and H.J. Patton , 2004. The 20-S Rayleigh wave attenuation tomography for Central and Southeastern Asia, *J. Geophys. Res*., 109, B12304, doi:10.1029/2004JB003193.

Yang, Y., and D.W. Forsyth (2006), Regional tomographic inversion of amplitude and phase of Rayleigh waves with 2-D sensitivity kernels, *Geophys.* J. Int., 166, 1148– 1160.

Yang, Y., M.H. Ritzwoller, A.L. Levshin, and N.M. Shapiro, 2007. Ambient noise Rayleigh wave tomography across Europe, *Geophys. J. Int.*, 168,p. 259 -274.

Yao, H., R.D. Van der Hilst, and M. V. De Hoop, 2006, Surface-wave array tomography in SE Tibet from ambient seismic noise and two-station analysis: I - Phase velocity maps, *Geophys. J. Int.*, 166, 732– 744.

Yoshizawa, K. and B.L.N. Kennett, 2002. Determination of the influence zone for surface wave paths, *Geophys. J. Int*., 149, 439-452.

Zhang, Y.S. & Tanimoto, T., 1992. Ridges, hot spots, and their interaction as observed inseismic velocity maps, *Nature*, 355, 45-49.

Zhang, Y.S. & Tanimoto, T., 1993. High-resolution global upper mantle structure and plate tectonics, *J. Geophys. Res*., 98, 9793-9823.

Zhou, Y., F.A. Dahlen, G. Nolet and G. Laske, 2005. Finite-frequency effects in global surface-wave tomography, *Geophys. J. Int.,* 163, 1087-1111.

Zhou Y., G. Nolet, F. A. Dahlen, G. Laske, 2006. Global upper-mantle structure from finite frequency surface-wave tomography, *J. Geophys. Res.*, 111, B04304, doi:10.1029/200.